A 3D reactive transport model for simulation of the chemical reaction process of ASR at microscale

Qiu, Xiujiao; Chen, Jiayi; Ye, Guang; De Schutter, Geert

Important note
To cite this publication, please use the final published version (if applicable).
Please check the document version above.

Contents lists available at ScienceDirect

Cement and Concrete Research

journal homepage: www.elsevier.com/locate/cemconres

A 3D reactive transport model for simulation of the chemical reaction process of ASR at microscale

Xiujiao Qiu [a,*], Jiayi Chen [b], Guang Ye [b], Geert De Schutter [a]

[a] *Department of Structural Engineering and Building Materials, Ghent University, Ghent, Belgium*
[b] *Department of Materials, Mechanics, Management & Design, Delft University of Technology, Delft, the Netherlands*

ARTICLE INFO

ABSTRACT

A 3D reactive transport model at microscale is proposed for simulating the chemical reaction process of alkali silica reaction (ASR) thermodynamically and kinetically including the dissolution of reactive silica, the nucleation and growth of ASR products and the dissolution of calcium hydroxide (CH) and calcium silicate hydrate (C-S-H) as a buffer of Ca^{2+} and OH^- to ASR. The implementation methodologies are firstly explained. Sensitivity analyses are done to calibrate some important parameters. The model is then applied to investigate the influence of the silica microstructural disorder degree on ASR. The simulation results show that the model is able to simulate successfully two typical patterns of the expansion sites location depending on the silica reactivity (inside the aggregate or in the aggregate-cement paste zone) found in field concrete and laboratory samples. A possible mechanism is provided based on the quantitative data captured by the model. The model can be extended to a multiscale ASR model for physic-chemical simulation to bridge the gap between the fundamental chemical mechanisms and the physical response of concrete.

1. Introduction

Concrete structures have been prone to deterioration by expansive alkali silica reaction (ASR) that causes extensive cracking thus reducing the safety of the whole structure. After decades of studies on the fundamental chemical mechanisms, it is widely known now that ASR starts from the dissolution of the reactive silica in the aggregate under the attack of OH^- and cations such as K^+, Na^+ that mainly come from the pore solution in the cement paste [1,2]. The dissolved silica further reacts with the Ca^{2+}, Na^+ and K^+ to form ASR products in the aggregate or/and in the cement paste. The resulting products include a high Ca/Si ratio gel and a low Ca/Si ratio gel [3]. It has reached to an agreement in literature that high Ca/Si ratio gel is less expansive than low Ca/Si gel [3–5]. Discoveries also show that high Ca/Si ratio gel usually locates near the aggregate-paste interface, while low Ca/Si ratio gel is likely found inside the aggregate relatively far from the aggregate-paste interface in some structures [6,7].

Based on at which level the ASR effect is implemented, the present ASR mechanical simulation models can be divided into two classes: models at concrete level and models at aggregate level. In the models at concrete level, the chemical reaction process is missing and the effect of

ASR is modelled directly by imposing an expansion strain in concrete. The change of the strain with time is derived from phenomenological laws or from reaction kinetic laws based on thermodynamic principles [8–11]. At aggregate level, three types of models can be found as concluded in [12]. In the first type of models, the effect of ASR is implemented into the model as an internal pressure directly at aggregate level, which is calculated based on the expansion test results [13–17]. In the second type of models, the effect of ASR is implemented into the model as a mass/volume of expansive reaction products. The reaction kinetics are functions of the change in mass or volume of the expansive alkali-silica gel. Then, the mass or volume change is used to calculate the internal strain or pressure that is imposed at aggregate level [18–22]. The chemistry and physics of ASR begin to be connected in this type of models at aggregate level. In the third type of models, the effect of ASR is implemented into the model also as a mass or volume of expansive reaction products produced. But the reaction kinetics of the mass or volume change of the reaction products are controlled by the ions diffusion into the aggregate [23–29]. Except for trying to build a connection between the chemistry and the physical response, the chemical process is taken into consideration with more fundamentals in this type of models at aggregate level. These mechanical predictive models are able to

provide an acceptable prediction about the pessimum size of aggregate or the structural mechanical degradation.

ASR is a multiscale phenomenon. The chemical reactions happen at a small level such as nanoscale or microscale (μm) depending on the pore size in cement paste. The cracking starts at a small scale and extends to a structural scale. Therefore, a comprehensive model should build the relation between the chemical reaction at a small scale and the physical response at a large scale, which means a multiscale modelling technique should be adopted in the model. More specifically, a model can be built firstly at a small scale to simulate the complicated chemical reaction process considering as much influential factors as possible. The simulation results then can be used at a large scale to simulate the cracking process and the mechanical degradation. Obviously, the models at concrete level can only predict the mechanical degradation at structural level since the chemical reaction mechanisms are not considered. Multiscale modelling technique has been adopted in the models at aggregate level with ASR effect being implemented at aggregate level and mechanical degradation at concrete analyzed. Especially in the third type of models at aggregate level, ion diffusion-reaction approach is used trying to take the chemical fundamentals into consideration. However, the reaction mechanisms are still not fully implemented in these models. For example, the ca^{2+} is not fixed in the expansive ASR gel, the chemical reactions are not thermodynamically controlled and the 'buffer effect' that during ASR the calcium hydroxide (CH) and calcium silicate hydrate (C-S-H) can dissolve to buffer the Ca^{2+} and OH$^-$, is not considered. What's more, a homogeneous sphere aggregate is adopted in most of the models, which is not consistent with the real situation that the reactive silica is actually heterogeneously distributed in the aggregate. Furthermore, due to the continuum approach adopted in these models, the present models are unable to describe the multiscale cracking development.

Our final goal is to build a comprehensive multiscale model as aforementioned. In this paper, a 3D reactive transport model at microscale for simulating the chemical reactions of ASR as comprehensively as possible is proposed. The chemical reactions including the dissolution of reactive silica and nucleation and growth of ASR products are simulated on the long term. In addition, the dissolution of CH and C-S-H to buffer Ca^{2+} and OH$^-$ for ASR is also considered. All of these chemical reactions are thermodynamic and kinetically controlled coupled with ion diffusion. Instead of assuming the aggregate to be an unrealistic homogeneous sphere, the microstructure of a reactive limestone considering heterogeneous reactive silica distributed following its realistic distribution is considered as an input together with the representative cement paste microstructure. The paper firstly elaborates the implementation methodologies. Then, sensitivity analyses are done to determine some important input thermodynamic and kinetic parameters. In the end, the model is applied to investigate the influence of the silica microstructural disorder degree on the location patterns of the ASR expansion sites. The investigation results show that the proposed model is not only able to simulate the discovered expansion sites pattern found in experiments or field concrete but also to provide a possible mechanism based on its capability of tracing the mass evolution of ASR products, the ion concentration evolution and the ion distribution on the long term.

2. Implementation methodology

2.1. Determination of the domain of interest

In order to simulate ASR as realistically as possible at microscale, the 3D microstructures of aggregate and cement paste are introduced in the model. A reactive siliceous limestone from Belgium was chosen as the reactive aggregate. Petrographic analyses on the thin-sections of this stone [30] showed that the alkali reactivity of this limestone attributes to the microcrystalline to cryptocrystalline silica and no other silica polymorphs were found. Computed tomography (CT) or focused ion beam milling combined with scanning electron microscopy (FIB-SEM) is

not applicable to obtain the 3D microstructure of the aggregate due to pixel size limitation. The microstructure of the aggregate was numerically simulated through Gaussian filtering method based on 2D scanning electron microscopy backscattered-electron (SEM-BSE) images. Pores below 1 μm in the aggregate are lost due to the voxel limitation. More details can be found in our former paper [30]. The final microstructure contains air voids (pore size over 1 μm), reactive silica and other nonreactive minerals. On the other hand, the cement paste microstructure with a water/cement (w/c) ratio of 0.4 in a REV size of $100 \times 100 \times 100 \ \mu m^3$ (voxel of 1 μm^3) was also numerical simulated using the cement hydration model of Chen and Ye extended from [31]. The cement properties used in the simulation are listed in Table 1. The simulated hydration degree α_{hy} is 78%. The simulated cement paste microstructure is composed by unhydrated clinker (C$_3$S, C$_2$S, C$_3$A, C$_4$AF), gypsum, insoluble phases in cement, saturated pores, CH, low density C1.1SH3.9, high density C1.5SH2, aluminate ferrite monosulfate (AFm) and katoite (C$_3$AH$_6$). The simulated pore solution ions are Ca^{2+}, OH$^-$, Na$^+$, K$^+$, H$_2$SiO$_4$$^{2-}$, Al(OH)$_4$$^-$, Fe(OH)$_4$$^-$, SO$_4$$^{2-}$. Only the first five ASR related ions are considered in this model.

No further hydration is considered in the model due to computer capability limitation. The average equivalent K$_{eq}$$^+$ concentration in the simulated cement paste was about 0.38 $mol \cdot L^{-1}$, with 0.35% Na$_2$Oe (mass of Na$_2$O and the equivalent transferred mass of K$_2$O) by mass of cement. Here, [K$_{eq}$$^+$] equals to the sum of the concentration of K$^+$ and the equivalent K$^+$ concentration of Na$^+$. Based on the empirical equation that relates the alkali concentration and alkali composition and the w/c ratio proposed by Helmuth [32], the alkalis in the cement is almost released completely to the pore solution with a hydration degree of 78% in the simulated cement paste.

The 3D domain of interest is shown in Fig. 1(a). The left cube is the cement paste while the right cube is the aggregate. The above mentioned phases are presented by different colors as explained in Fig. 1(b). The final voxel size of the simulation is reset to be 2 μm considering that the minimum reactive silica particle in the selected limestone is bigger than 2 μm [30]. The final domain size becomes $50 \times 100 \times 50$ with one node representing a volume of 8 μm^3. This process has further reduced the air voids fraction in the aggregate. Thus, the diffusion of an ion in the aggregate was implemented by assigning a calculated diffusion coefficient to the whole aggregate based on the mercury intrusion porosimetry (MIP) results as stated in the next section.

2.2. Ions transport

The anisotropic diffusion of pore solution ions is simulated using the multi-relaxation time (MRT) lattice Boltzmann method instead of the most popular Bathnagar-Gross-Krook (BGK) method [33]. The MRT model provides the advantage over BGK that the artificial error dependent on the relaxation time is suppressed [34], especially for the case in which the diffusion coefficients vary spatially. This method requires only seven velocities in three dimensions. The method is not elaborated here due to the space limitation. More details can be found in [35]. The diffusion coefficients of different ions in different phases are different. In the model, ions are considered to diffuse within pores, low density C1.1SH3.9, high density C1.5SH2, aggregate and ASR products. Due to the incomplete pore information in the aggregate, ions are assumed to be able to diffuse in the aggregate with theoretical calculated diffusion coefficients. Table 2 summarizes the diffusion coefficients of [Ca^{2+}, OH$^-$, Na$^+$, K$^+$, H$_2$SiO$_4$$^{2-}$] in the above physical phases. The diffusion coefficient of an ion in the aggregate D_{agg} is calculated using the empirical equation $D_{agg} = D_w \phi^{3.05}$ from Mihara et al. [36]. ϕ is the porosity of the aggregate obtained from MIP, which is 0.8% in our case. The calculated diffusion coefficients of [Ca^{2+}, OH$^-$, Na$^+$, K$^+$, H$_2$SiO$_4$$^{2-}$] in the aggregate D_{agg} are then 4×10^{-7} times D_w, where D_w are the diffusion coefficients of these ions in pore water as shown in Table 2.

During simulation, the simulation time per step Δt is calculated by:

Table 1
Details of the simulated cement paste domain.

Cement compositions, wt%							Simulated w/c ratio	Simulated α_{hy}, %
C$_3$S	C$_2$S	C$_3$A	CaSO$_4$	C$_4$AF	K$_2$SO$_4$	Na$_2$SO$_4$		
64.1	13	7.9	4.4	8.1	1.3	0.3	0.4	78

(a)

(b)

13 Non-reactive minerals
12 Reactive silica
11 C1.5SH2
10 C3AH6
9 AFm
8 CH
7 C1.1SH3.9
6 Insoluble in cement
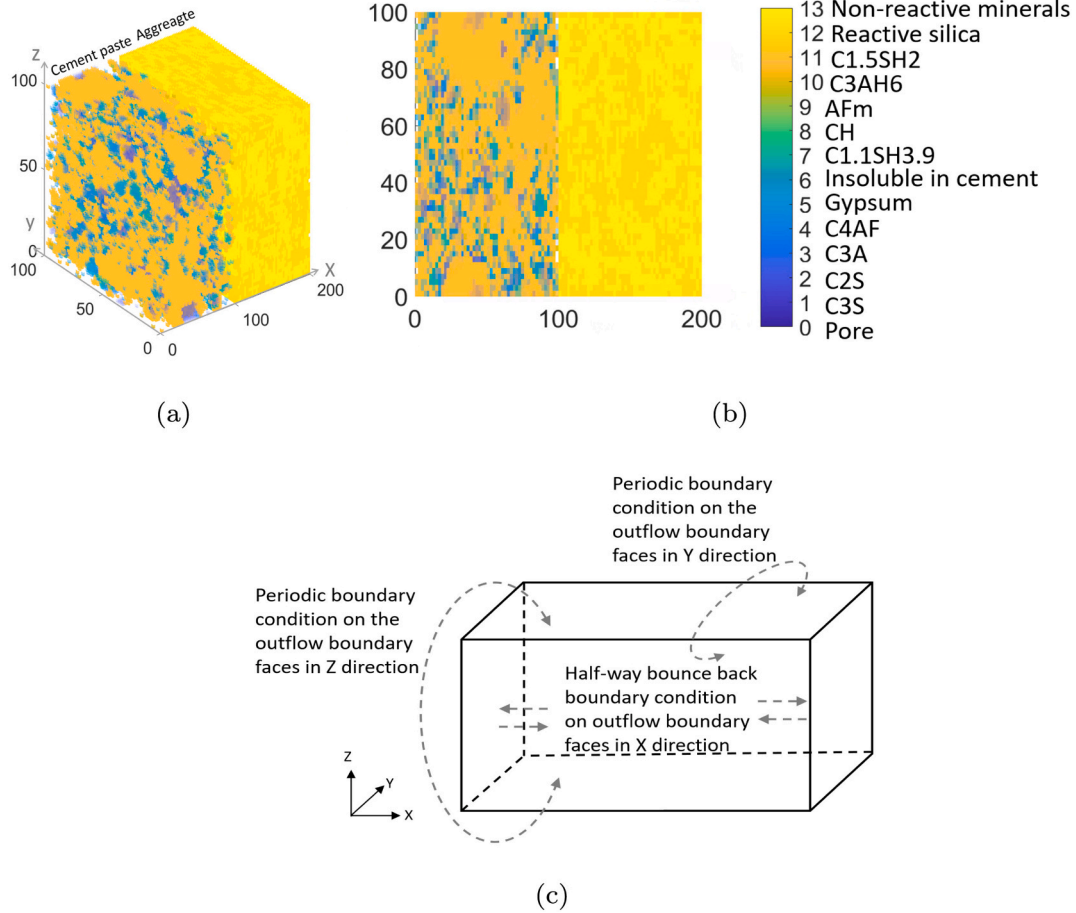5 Gypsum
4 C4AF
3 C3A
2 C2S
1 C3S
0 Pore

(c)

Fig. 1. **(a)**: A schematic diagram of the initial 3D domain of interest in the model. The left of the cube is cement paste and the right of the cube is aggregate. Different colors represent different phases. Unit of scale: μm; **(b)**: A 2D slice from the 3D domain; **(c)**: Boundary conditions applied on the outflow faces of the domain.

Table 2
Diffusion coefficients of ASR related ions in different phases.

Phase	Diffusion coefficients, m^2/s
Pore (D_w)	$[0.72(Ca^{2+}), 5.30(OH^-), 1.33(Na^+), 1.80(K^+), 0.70 (H_2SiO_4^{2-})] \times 10^{-9}$ [37]
Low density C1.1SH3.9 (D_{LD})	$\frac{1}{80}D_w$ [31]
High density C1.5SH2 (D_{HD})	$\frac{1}{720}D_w$ [31]
Low Ca/Si ASR product (D_{KSH})	$\frac{1}{80}D_w$
High Ca/Si ASR product (D_{TobH})	$\frac{1}{720}D_w$
Aggregate (D_{agg})	$4 \times 10^{-7} D_w$

$$\Delta t = \frac{T_P}{T_{LB}} \tag{1}$$

where T_{LB} is the total simulation steps and T_P is the physical target simulation time. T_{LB} can be calculated by Eq. (2), which describes that the concentration flux F_o of an ion is not changed when being simulated

in a lattice Boltzmann domain. L_{LB} is the length of lattice domain (100), and D_P is the physical diffusion coefficient of the fastest ion (OH^- in this model) in the dominant phase (high density C1.5SH2). L_P is the real physical length of the simulation domain (200 μm). D_{HB} is the artificial diffusion coefficient of OH^- in the high density C1.5SH2 in the lattice domain and is determined by the input relaxation time τ via Eq. (3). δx and δt are the unit lattice spacing and unit time step respectively. Based on D_{HB}, the diffusion coefficients of other ions in different phases in the lattice domain can be determined through the coefficient ratio which can be calculated using the data in Table 2.

$$\frac{D_P T_P}{L_P^2} = F_o = \frac{D_{HB} T_{HB}}{L_{LB}^2} \tag{2}$$

$$D_{HB} = \frac{1}{3}\left(\tau - \frac{1}{2}\right)\frac{\delta x^2}{\delta t} \tag{3}$$

During ion diffusion, a half-way bounce back boundary condition [33] is applied to the crystal phases and the unhydrated cement in the cement paste which prevents ions from diffusing through these phases but bounces back to the coming direction. A periodic boundary condition [33] is applied on the outflow boundary faces in *Y* and *Z* direction,

which permits ions to diffuse through the surface of the simulation box and diffuse back to the simulation box through the opposite surface in the same orientation. The half-way bounce back boundary condition is applied on outflow boundary faces in X direction of the domain of interest that prevents ions from diffusing through the surfaces but bounces back to the box. As such, the outflow perturbs the system as little as possible and the mass balance is obeyed. These different boundary conditions are shown in Fig. 1(c).

2.3. Dissolution of reactive silica

As illustrated by Powers and Steinour [3], ASR starts from the dissolution of the reactive silica after the hydroxide ions progressively attack the silanol bonds ($\equiv$SiO–OH) that are present at the silica-water interface, which results in the formation of H_4SiO_4. In basic solution, H_4SiO_4 further decomposes to $H_3SiO_4^-$ and $H_2SiO_4^{2-}$. In high pH pore solution, it mainly decomposes to $H_2SiO_4^{2-}$ [38]. The dissolution rate of silica is kinetically affected by many factors as concluded by Kim et al. in [39] including reactive silica surface area, reaction temperature, pH of pore solution, ionic strength of pore solution and under-saturation degree of silica. An integrated dissolution kinetic law considering all of the above influencing parameters was proposed in [39] and is adopted in our work as shown in Eq. (4).

$$R_{SiO_2} = -\frac{dSiO_2}{dt} = \frac{\rho'_{SiO_2}}{\rho_{SiO_2}} A exp\left(-\frac{E_a}{RT}\right)$$
$$\times (\alpha_{OH^-})^{0.5} I^{0.2}\left(1 - \frac{Q_{SiO_2}}{K_1}\right) \quad (4)$$

where R_{SiO2} is the dissolution rate of the reactive silica, $m \cdot s^{-1}$; $dSiO_2$ is the thickness of the dissolved silica, m; dt is the simulated time, s; ρ_{SiO2}' is the mass of reactive silica per mol, 0.06 $kg \cdot mol^{-1}$; ρ_{SiO2} is the density of the reactive silica, which varies from 2150 to 2650 $kg \cdot m^{-3}$ depending on the silica polymorphs. 2550 $kg \cdot m^{-3}$ is used for the reactive microcrystalline to cryptocrystalline silica in the limestone used in this work; A is the pre-exponential factor, $mol \cdot m^{-2} \cdot s^{-1}$; E_a is the activation energy of surface controlled silica dissolution, $J \cdot mol^{-1}$; R is the gas constant, 8.314 $J \cdot K^{-1} \cdot mol^{-1}$; T is the temperature. 298.15 K is considered in the model; I is the ionic strength of the pore solution; K_1 is the equilibrium constant of reactive silica dissolution; α is the activities of ions, which is calculated using Extended-Debye-Huckel equation; Q_{SiO2} is the reaction quotient, calculated by $Q_{SiO_2} = \frac{\alpha_{H_2SiO_4^{2-}}}{\alpha_{OH^-}^2 \alpha_{SiO_{2(s)}}}$.

2.4. Dissolution of CH and C-S-H

According to Wang and Gillott [40] and Guthrie et al. [41], CH and C-S-H act as a 'buffer' to maintain a high pH value and provide Ca^{2+} and OH^- ions for further reaction during ASR. Thus, CH and C-S-H are also considered to dissolve in the model according to their local thermodynamic state during each simulation step. Dissolution happens when the solution for CH or C-S-H is undersaturated.

For CH dissolution the kinetic law from [42] as defined by Eq. (5) is adopted. The equation has considered the forward and backward reaction at 25°C as well as the influence of Ca^{2+} and OH^-.

$$R_{CH} = -\frac{dCH}{dt} = \frac{\rho'_{CH}}{\rho_{CH}}\left(k_f - k_b \alpha_{Ca^{2+}} \alpha_{OH^-}^2\right) \quad (5)$$

where R_{CH} is the dissolution rate of CH, $m \cdot s^{-1}$; dCH is the thickness of dissolved CH, m; ρ_{CH}' is the mass of CH per mol, 0.074 $kg \cdot mol^{-1}$; ρ_{CH} is the density of CH, 2200 $kg \cdot m^{-3}$; k_f is the forward dissolution rate of CH, $1.55 \times 10^{-4} mol \cdot L^{-1} \cdot s^{-1} \cdot m^{-2}$; k_b is the backward precipitation rate of CH, 41 $L^2 \cdot mol^{-2} \cdot s^{-1} \cdot m^{-2}$.

For C-S-H dissolution, the method used in [41] is adopted that a dissolution rate constant is used, which is determined as the dissolution

rate of the Ca-Si minerals that is structurally and compositionally similar to C-S-H in the database of Palandri and Kharake [43]. The dissolution equations of C-S-H in cement paste are presented in Table 3 and the dissolution kinetics law is defined by Eq. (6).

$$-\frac{dmole_{Si}}{dt} = R_{C-S-H} \quad (6)$$

where R_{C-S-H} is the Si releasing rate due to the dissolution of C-S-H, and $dmole_{Si}$ is the mole change of the released Si. A constant value for R_{C-S-H} of 3×10^{-11} $mol_{si} \cdot s^{-1} \cdot m^{-2}$ from [41] is used in the model.

2.5. Surrogate of ASR products

In 2019 Leemann et al. [44] have investigated the reaction sequence of ASR by adding caesium to concrete. The results implicated that it is the formation of the amorphous ASR products near the surface of the aggregate that causes the initial expansion of the structure. They have also characterized the chemical compositional difference of the amorphous and crystalline ASR products formed in concrete by using Raman microscopy [45]. The average Ca/Si ratio and alkali/Si ratio of these two products are very similar, while the main difference concerns the Na/K ratio with higher values in the amorphous products compared to the crystalline ones. This is similar to discoveries made by Shi et al., who have synthesized three crystal alkali-silica reaction products (K-shlykovite, Na-shlykovite and ASR-P1) identical to that formed in field concrete [46]. The study of Shi et al. also showed that the temperature has an influence on the products formed. Under 40°C, only crystalline K-shlykovite and amorphous products are formed [47].

Based on the above studies, the K-shlykovite ($KCaSi_4O_8(OH)_3 \cdot 2.9H_2O$, KSH) is used as the surrogate for the low Ca/Si ratio amorphous ASR products in our model when the temperature is 25°C. The Na^+ is transferred to an equivalent mass of K^+ in the model based on the fact that most of the alkalies in the pore solution of concrete are K^+ and they behave kinetically similarly in ASR system [48]. Another product implemented in the model is the tobermorite ($(CaO)_{0.6667}SiO_2 \cdot 1.5H_2O$, TobH) as TobH also presents in ASR-damaged concrete and Shi et al. [46] also found it during their synthesis process.

2.6. Nucleation and growth of ASR products

2.6.1. Nucleation kinetic law

Due to lacking of the kinetic information about the nucleation and growth of ASR products, the classical nucleation and growth theory is adopted in the model. According to the theory, ASR products begin to nucleate when the local solution reaches a thermodynamic supersaturation state. The dependence of the nucleation rate R_n ($m^{-3} \cdot s^{-1}$) on the supersaturation degree S can be described by Eq. (7) [49].

$$R_n = A_n S exp\left(-\frac{B_n}{ln^2 S}\right) \quad (7)$$

The kinetic parameter A_n ($m^{-3} \cdot s^{-1}$) is defined as,

$$A_n = \left(\frac{4\pi}{3v_0}\right)^{1/3}\left(\frac{\sigma}{k_B T}\right)^{1/2} D \quad (8)$$

and the thermodynamic parameter B_n is defined as,

$$B_n = \frac{fv_0^2 \sigma^3}{(k_B T)^3} \quad (9)$$

S is the supersaturation degree calculated locally according to the solution environment. v_0 (m^3) is the volume of a molecule of the new formed phase; σ is the interfacial energy ($J \cdot m^{-2}$), which is the free energy per unit area of the nucleus interface. D is the apparent diffusion coefficient of the solute species ($m^2 \cdot s^{-1}$). f is the shape factor, for a sphere $f = 16$, for a cube $f = 32$. $k_B T$ is the thermal energy with k_B being

Table 3
The determined equilibrium constant for thermodynamic simulations.

	Chemical reaction formula	Equilibrium constant
Silica dissolution	$SiO_{2(s)} + 2OH^- \rightarrow H_2SiO_4{}^{2-}$	$logK_1 = -3.73$
CH dissolution	$Ca(OH)_2 \rightarrow Ca^{2+} + 2\ OH^-$	$logK_2 = -5.2$
C-S-H Dissolution	$Ca_{1.1}SiO_2(OH)_{2.2} \cdot 2.8H_2O \rightarrow 1.1Ca^{2+} + H_2SiO_4{}^{2-} + 0.2OH^- + 2.8H_2O$	$logK_3 = -7.85$
	$(CaO)_{1.5}SiO_2 \cdot 2H_2O \rightarrow 1.5Ca^{2+} + H_2SiO_4{}^{2-} + OH^- + 0.5H_2O$	$logK_4 = -11.46$
KSH formation	$Ca^{2+} + K^+ + 4H_2SiO_4{}^{2-} + 2.9H_2O \rightarrow KCaSi_4O_8(OH)_3 \cdot 2.9H_2O + 5OH^-$	$logK_5 = -12$
TobH formation	$0.6667Ca^{2+} + H_2SiO_4{}^{2-} + 0.8333H_2O \rightarrow (CaO)_{0.6667}SiO_2 \cdot 1.5\ H_2O + 0.6667\ OH^-$	$logK_6 = -5.33$

the Boltzmann constant (1.38×10^{-23}, $J \cdot K^{-1}$).

The location of the nucleus of ASR products in the domain is simulated based on the probability distribution theory that at a constant supersaturation degree, the appearance of a nucleus can be regarded as a random process and as independent. The probability P_n of forming n nucleus in a time interval Δt in a volume V can be described by the Poisson distribution [50] as presented by Eq. (10).

$$P_n = \frac{N^n}{n!}exp(-N) \qquad (10)$$

N is the average number of the newly formed nucleus in time δt and in a volume V, which can be calculated by Eq. (11).

$$N = R_n V \Delta t \qquad (11)$$

2.6.2. Growth kinetic law

Once a nucleus is formed, ASR products will grow if the local solution is supersaturated. The growth rate R_g ($m \cdot s^{-1}$) is modelled using the diffusion-reaction theory (power law) [51] based on the experience of Andalibi et al. [52] who simulated the nucleation and precipitation of C-S-H matching the experimental data in a simplified chemical system. The growth rate is presented by Eq. (12).

$$R_g = k_g exp\left(-\frac{E_g}{RT}\right) K_e{}^v \left(S^{1/v} - 1\right)^g \qquad (12)$$

where k_g, E_g, v, g are the growth constant ($m \cdot s^{-1}$), the growth activation energy ($J \cdot mol^{-1}$), the total number of ions produced by one of the formula units of solid upon dissolution [52,53], and the growth order respectively. K_e is the equilibrium constant of the new formed phase.

During the simulation, three types of non-full nodes are available for ASR products to nucleate and grow. Type 1 is the pore nodes. Type 2 is the non-full nodes in the cement paste and type 3 is the partially dissolved silica nodes in the aggregate. Once a non-full node is full of ASR product, the extra mass is evenly relocated to the non-full nodes from its 26 adjacent nodes. If there is no more non-full adjacent node, the extra ASR product is then accumulated in the full node.

2.7. Input thermodynamic and kinetic parameters

2.7.1. Thermodynamic parameters

Six chemical reactions are involved in the model including silica dissolution, CH dissolution, low density and high density C-S-H dissolution, KSH formation and TobH formation. Table 3 summarizes the equilibrium constants for the thermodynamic simulations. Except the equilibrium constant of KSH formation K_5, all equilibrium constants are collected from [54]. K_5 is obtained through sensitivity analysis which is stated in Section 3.2 due to lacking data in literature. K_1 is the solubility of silica in the water. It should be noticed that the dissolution equilibrium constant of silica in water increases as the silica microstructural disorder increases. For the reactive silica (cryptocrystalline to microcrystalline quartz) contained in the limestone in this paper, a value of ($1 \times 10^{-3.73}$) is used. Considering the fact that the solubility of silica is greatly affected by the pH of the pore solution due to ionization, K_1 is then modified in the model according to the local pH based on the

ionization reactions [38]. It is observed that at high pH, the solubility of silica increases by several orders of magnitude.

2.7.2. Kinetic parameters

Table 4 summarizes the determined kinetic parameters from silica dissolution to the growth of ASR products in the model.

For the silica dissolution parameters in Eq. (4). The activation energy E_a varies from 9000 $J \cdot mol^{-1}$ to 6000 $J \cdot mol^{-1}$ in literature depending on the silica microstructural disorder [55]. A value of 78000 $J \cdot mol^{-1}$ from [56] is adopted for the reactive micro-to-crypto crystalline silica in the model. For the pre-exponential constant A, the dissolution rates of the reactive silica at different temperatures should be tested to determine it as elaborated in [56]. In our model, the value of 5.5×10^{-3} $mol \cdot m^{-2} \cdot s^{-1}$ from [39] is adopted.

For the nucleation parameters in Eqs. (8) and (9), the molecular volume v_0 of 0.25 nm^3 for TobH is obtained from literature [57]. For KSH, v_0 of 0.323 nm^3 is taken as the molecular volume of shlykovite since its crystal form highly resembles the structure of shlykovite. The interfacial energy σ, which is the free energy per unit area of the nucleus interface, is 12 $mJ \cdot m^{-2}$ for TobH [57]. However for σ of KSH, there is a lack of experimental data. A recent finding [58] has revealed that the formation of C-S-H proceeding via a complex two-step pathway. In the first step, amorphous spheroids whose composition is deleted in calcium and charge compensated with alkalis such as sodium or potassium are formed. In the second step, calcium exchanges part of the sodium or potassium in the amorphous spheroids and these amorphous spheroids then aggregate to the final C-S-H. Based on this finding, it is reasonable to believe that the formation process of KSH is similar to C-S-H especially the first step where nucleation happens. In the second step, for KSH less calcium concentration would be exchanged due to its low concentration in the pore solution. Therefore, it is reasonable to assign the same interfacial energy (12 $mJ \cdot m^{-2}$) of the nucleus of C-S-H to that of KSH. The apparent diffusion coefficients D for KSH and TobH are then estimated using the Stokes–Einstein relationship [51] based on their molecular volume and the interfacial energy, which are 9.07×10^{-10} and $9.66 \times 10^{-10} m^2 \cdot s^{-1}$ respectively.

For the growth parameters in Eq. (12), the growth constant K_g, the growth activation energy E_g, the growth order g of TobH are collected
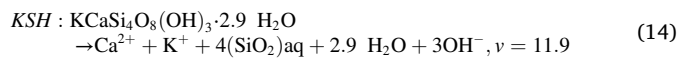
Table 4
The determined kinetic parameters for kinetic simulations.

Chemical reaction process	Parameters	Value	
		KSH	TobH
Silica dissolution	A	5.5×10^{-3}, $mol \cdot m^{-2} \cdot s^{-1}$	
	E_a	78000, $J \cdot mol^{-1}$	
Nucleation of ASR products	v_0	0.323, nm³	0.25, nm^3
	σ	12, $mJ \cdot m^{-2}$	12, $mJ \cdot m^{-2}$
	D	9.07×10^{-10}, $m^2 \cdot s^{-1}$	9.66×10^{-10}, $m^2 \cdot s^{-1}$
Growth of ASR products	K_g	16.67, $m \cdot s^{-1}$	8.333×10^{-6}, $m \cdot s^{-1}$
	E_g	330, $J \cdot mol^{-1}$	330, $J \cdot mol^{-1}$
	g	1	1
	v	11.9	3.8334
	f	16	16

from the extended cement hydration model of [31] with value $8.333 \times 10^{-6} \ m \cdot s^{-1}$, $330 \ J \cdot mol^{-1}$ and 1 respectively. However, for KSH no data is available in literature. Thus, in order to reduce the number of parameters, the growth constant K_g is used to control the growth of KSH and the other parameters are fixed. Similar to σ, the growth activation energy E_g, the growth order g of KSH are assumed to equal to those of TobH. Sensitivity analysis on K_g of KSH has been done to see its influence on ASR as stated in Section 3.3. A final value of 16.67 m/s is adopted. The shape factor f is 16 for both KSH and TobH assuming their nucleus are spherical based on [58].

The parameter v is the total number of ions produced by one of the formula units of solid upon dissolution [53]. For an ionic-crystal solid, v is a constant which is the sum of the stoichiometric number of the dissolved ions in the solute formula. However, for amorphous solid like C-S-H and ASR products, v is not a constant and depends on the dissolution formula adopted. For example, values of 5/2 and 2 for C-S-H have been used in [59,60] respectively. In our work, the dissolution of KSH and TobH in water are considered and shown below:

$$TobH : (CaO)_{0.6667}SiO_2 \cdot 1.5 \, H_2O$$
$$\rightarrow 0.6667 \, Ca^{2+} + (SiO_2)aq + 0.8333 \, H_2O + 1.3334 \, OH^-, v = 3.8334 \tag{13}$$

$$KSH : KCaSi_4O_8(OH)_3 \cdot 2.9 \ H_2O$$
$$\rightarrow Ca^{2+} + K^+ + 4(SiO_2)aq + 2.9 \ H_2O + 3OH^-, v = 11.9 \tag{14}$$
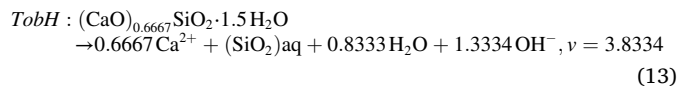
where aq means aqueous. Therefore, v is 3.8334 for TobH and 11.9 for KSH. On the other hand, our simulation results show that the influence of v on the growth rate of the new phase is not significant because a large growth rate is applied as determined in Section 3.3.

3. Sensitivity analyses

As stated before, sensitivity analyses have been done on the equilibrium constant K_5 of KSH, which determines the thermodynamic state of the solution for KSH to be formed and the growth constant K_g of KSH, which determines how fast ASR products formation consumes the ions in the solution. Another parameter τ, which determines the physical time for a target simulation time, is also studied. The relaxation time τ is firstly discussed below as it is the basis for the other simulations.

3.1. The relaxation time

The relaxation time τ is a transport parameter that determines how quickly the diffusion process evolves to the theoretical equilibrium state which relates to the lattice kinematic viscosity of fluid. Eqs. (3), (2) and (1) show that the simulation time step Δt increases as τ increases, which means that the number of iterations for simulating a given time decreases as τ increases. On the other hand, the simulation accuracy of ions diffusion, which is determined whether the ion reaches its theoretical equilibrium concentration after one step, decrease as τ increases. Studies have shown that in BGK scheme, τ should be selected in a range (0.5, 5] [33,61], while in MRT scheme, τ can be set as high as 100 for predicting effective diffusivity of porous media [34]. Since ASR happens in few years or decades in the field, a suitable τ should be determined to find a balance between the number of iterations (not being too large) and ions diffusion accuracy (within an acceptable range). Thus, four τ (12, 1200, 12,000, 24,000) were studied in the lattice domain where an initial average concentration of Ca^{2+} and K_{eq}^+ of 20 $mmol \cdot L^{-1}$ and 0.2 $mol \cdot L^{-1}$ (see in Section 3.2.1 about how it is determined) in the cement paste are adopted respectively. Based on [34], among different τ, 12 is considered to be the reference τ that could simulate the ions diffusion accurately. The resulting Δt were 2 s, 3.6 min, 36 min and 72 min per simulation step respectively. In order to avoid the influence of chemical reactions on the ions diffusion, all the chemical reactions are not implemented in the simulations for this section.

Fig. 2 shows the concentration evolution of Ca^{2+} along X axis at four different points (1 h, 12 h, 1 day and 6 days) in the lattice domain with different τ used. The Y axis is the average concentration of an ion on each YOZ plane, which was calculated as the average concentration of each ion in the nodes where the ions can diffuse into on each YOZ plane. The X axis is the distance of each YOZ plane to the most left one where X = 0. The black dashed line distinguishes the cement paste zone and aggregate zone. It can be seen from the figure that the blue line (reference line) and red line ($\tau = 1200$) are almost overlapped at each time points, while the black line ($\tau = 12000$) and green line ($\tau = 24000$) varies much from the blue line. This means that the simulated ion diffusion accuracy can be guaranteed as long as $\tau \leq 1200$. However, when τ reaches 12,000 or higher, the deviations from the predicted theoretical diffusion become too large. Fig. 3 further confirms the conclusion with the K_{eq}^+ concentration distribution at different time points in the domain with different τ.

Based on the simulation results, a value of 1200 for τ, which resulting a simulation time step Δt of 3.6 min, is used in the model. Values between 1200 and 12000 are not considered as a small variation begins to occur when $\tau = 1200$ as shown in Figs. 2(c), 3(b) and (c).

3.2. The equilibrium constant of KSH

3.2.1. Inputs of the model

In our former paper [30], five 3D representative microstructures with a size of $(100 \times 100 \times 100 \ \mu m^3)$ of the siliceous limestone have been simulated based on the real heterogeneous distribution of the minerals at microscale. Each microstructure contains a different silica fraction (volume fraction of silica in the aggregate from 6.58% to 40.91%) and distribution pattern. In this section, the microstructure with the highest silica fraction (about 40.91%) was used. The reactive silica is the slowly-reactive one. The simulated cement paste as described in Section 2.1 was used. The initial average concentration of Ca^{2+} was around 20 $mmol \cdot L^{-1}$. A relative high Ca^{2+} concentration is chosen to give a full picture about the role of calcium during ASR. The described thermodynamic and kinetic parameters of Tables 3 and 4 were used, except K_5 of KSH, of which the sensitivity to be studied. τ is set to 1200.

Alkali concentration of cement paste is the results of clinker composition, w/c ratio, and degree of hydration reaction. The original average equivalent K_{eq}^+ concentration in the simulated cement paste was about 0.38 $mol \cdot L^{-1}$, with 0.35% Na$_2$Oe (mass of Na$_2$O and the equivalent transferred mass of K$_2$O) by mass of cement. We have decreased the K_{eq}^+ concentration artificially to an average value of 0.2 $mol \cdot L^{-1}$ (Na$_2$O$_e$% around 0.14%) while its distribution was kept. The distribution of the ions wouldn't change much since the clinker composition is almost not changed by the small percentage of Na$_2$O$_e$. Therefore, instead of changing the clinker composition and redo the simulation to obtain the cement paste, we have artificially changed the concentration of K_{eq}^+ in the aforementioned simulated cement paste to the corresponding concentration while its spatial distribution was maintained. A low alkali concentration was chosen because it was easier or shorter for the system to reach its equilibrium state.

In literature, higher threshold alkali concentrations to trigger ASR induced damage have been reported. For example, 0.22 $mol \cdot L^{-1}$ was proposed in [62] with silica fume used and in [63] a highly reactive Jobe sand used. 0.65 $mol \cdot L^{-1}$ was found in [64] and in [65] with reactive siliceous limestone used. However, it should be noticed the threshold alkali concentration for expansion is different from the threshold alkali concentration to trigger the formation of ASR products. The former one is larger than the latter one. A threshold alkali concentration of 0.2 $mol \cdot L^{-1}$ below which no ASR products can be formed was reported in [48] based on their thermodynamic simulation results with a temperature of 55 °C. In our model, with a temperature of 25 °C, a threshold value of around 0.16 $mol \cdot L^{-1}$ was found. Mechanisms have been reported to explain the discrepancy. According to bažant [23], a limited amount of
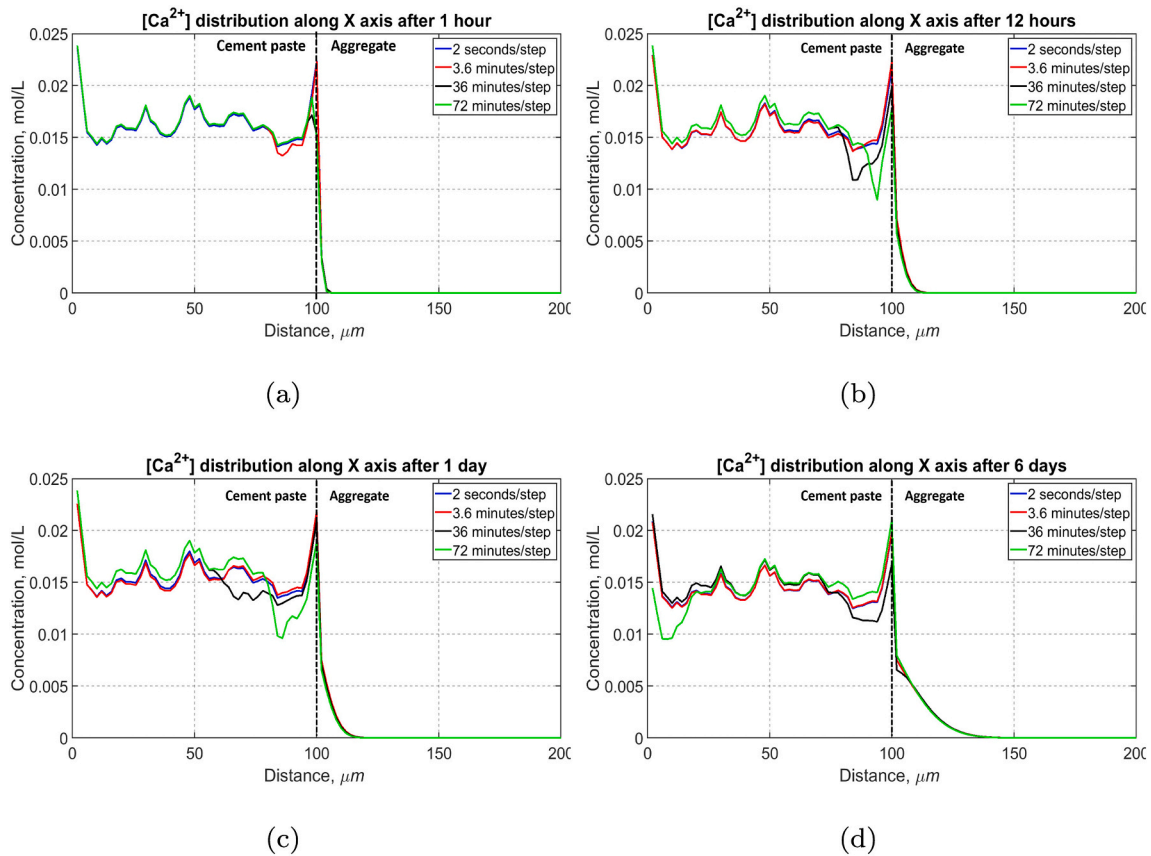
Fig. 2. The evolution of Ca^{2+} concentration distribution along X axis at different time points within 6 days in the same system but different τ. Only ions diffusion is implemented in the system.

ASR products will cause no damage when there are enough pore space to accommodate them. On the other hand, our simulations that explores the influence of different alkali concentrations (0.2, 0.38, 0.5, 0.75 $mol \cdot L^{-1}$) on the chemical reaction sequence and ASR products location, show that alkali concentration does not affect both except that the formation rate of ASR products is decreased as the concentration decreases (the results are not presented due to space limitation), which is consistent with the experimental results of [48]. Thus, the adoption of a small alkali concentration in the model can output the same information about ASR as the adoption of a high alkali concentration.

3.2.2. Simulation results

Six different values varying from 1×10^{-8} to 1×10^{-18} for K_5 were studied. The simulated mass evolution of KSH and TobH (represented by M_V, $kg \cdot m^{-3}$) within 270 days is shown in Fig. 4. Here, M_V is the normalized mass per cubic meter that equals to the total mass of the formed phase divided by the total volume of the simulated domain which is 1×10^{-12} m^3. The navy blue curves in both of the subfigures indicate that when $\log K_5 \geq -8$, there is no KSH but only TobH formed in the domain. However, when $\log K_5 \leq -16$ as indicated by the black and rose red curves (overlapping with the black curve) in both of the subfigures, the situation is the opposite with no TobH but only KSH formed in the domain.

In order to verify whether the alkali concentration is not large enough for KSH to form when $\log K_5 \geq -8$, simulations were repeated with the initial equivalent K_{eq}^+ concentration artificially increased to 0.38, 0.50 and 0.75 $mol \cdot L^{-1}$ for $\log K_5 = -8$. The simulation results are shown in Fig. 5. As can be seen the produced KSH is still at an order of 1×10^{-3} $kg \cdot m^{-3}$ even $[K_{eq}^+]$ is as high as 0.75 $mol \cdot L^{-1}$, while the produced amount TobH is large (7 $kg \cdot m^{-3}$).

Ca^{2+} plays a significant role in the initial sequence of ASR. Based on a simple chemical reactor composed by high NaOH solution, silica fume and CH, the studies of Hou et al. [66,67] and Kim and Olek [39,68] have proposed that C-S-H is formed firstly and ASR products is not formed until Ca^{2+} is depleted by C-S-H at different temperatures (23°C, 38°C and 55°C). Recently, Kim et al. [69] has confirmed this hypothesis in a model reactant system with one reactive aggregate exposed to high alkali concentration at 60 °C. The study of Li et al. [70] also discovered an absence of CH in the vicinity of the reactive aggregate in the mortar samples at 23°C. These researches indicate that when relatively high concentration of Ca^{2+} is present near to the reaction sites in aggregate, C-S-H will be formed and temperature does not affect the chemical fundamentals of ASR but only its kinetics rate as also confirmed by numerous researchers [56,71,72]. Therefore, the above analyses indicate that when the temperature is 25°C, the equilibrium constant for KSH should be less than 1×10^{-8} while greater than 1×10^{-16} based on the fact that the Ca^{2+} concentration in the domain is relatively high (20 $mmol \cdot L^{-1}$) and is distributed all over the cement paste so that both ASR products and C-S-H should be formed. To further calibrate the value between 1×10^{-10}, 1×10^{-12} and 1×10^{-14}, some random slices with distributions of TobH were extracted from the 3D domain with the above three different equilibrium constants used respectively (0.2 $mol \cdot L^{-1}$ initial alkali concentration), which are presented in Fig. 6. In the subfigures, the red dashed line distinguishes the cement paste zone and the aggregate zone. It can be seen that part of TobH is always located in the aggregate, near the aggregate-cement paste interface in all of the subfigures. However, the amount of TobH inside the cement paste decreases with K_5 decreasing. When $\log K_5 = -14$, there is no TobH in the cement paste. When $\log K_5 = -10$, most of TobH is in the cement paste. Considering the discovery from [45,69] that high Ca/Si ASR products are found mostly inside the aggregate near the aggregate-cement paste interface and in the ITZ zone, a middle value of 1×10^{-12} is chosen for
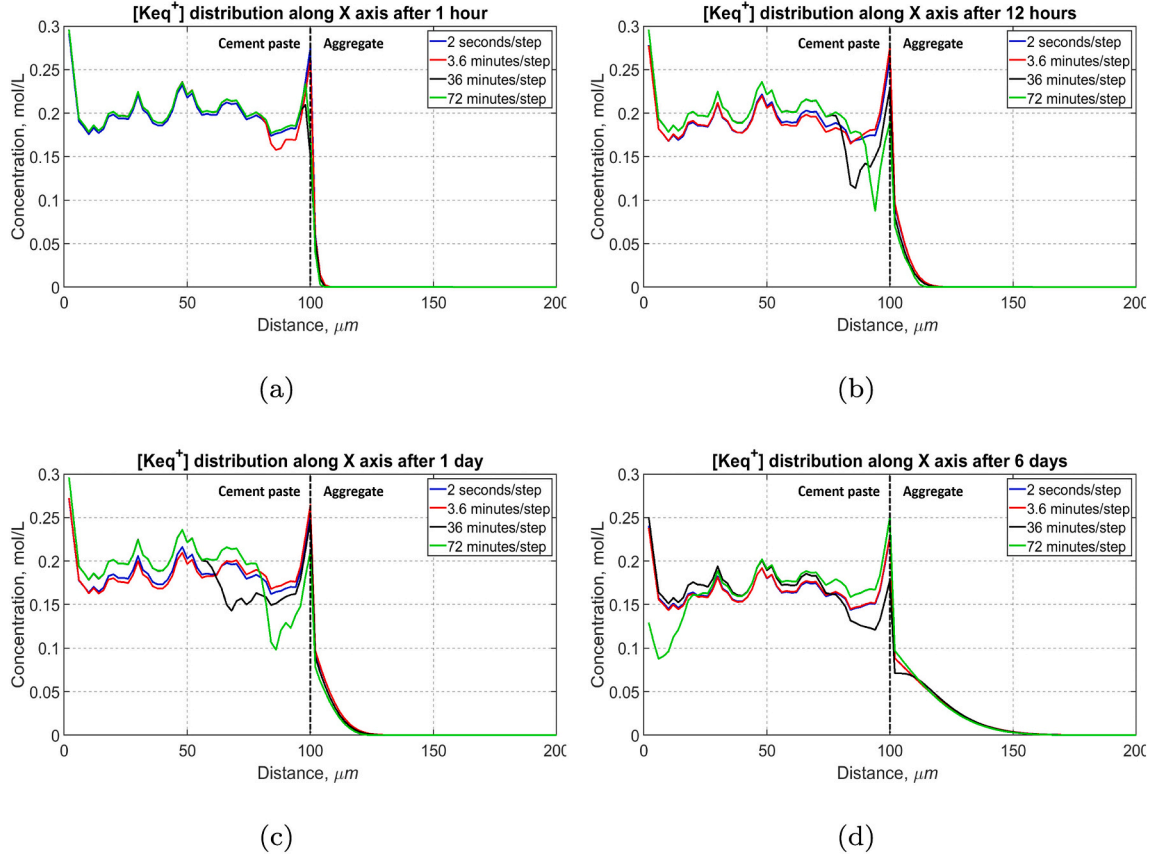
Fig. 3. The evolution of K_{eq}^+ concentration distribution along X axis at different time points within 6 days in the same system but different τ. Only ions diffusion is implemented in the system.
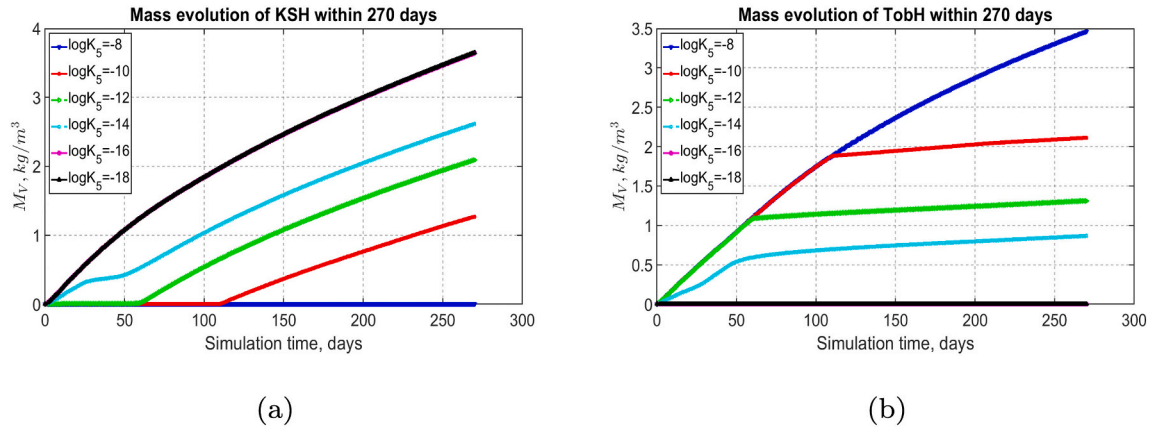

Fig. 4. The mass evolution represented by M_V of ASR products in the domain with different K_5 used within 270 days. (**a**): The mass evolution of KSH; (**b**): The mass evolution of TobH.

K_5 in the model.

It should be noticed that in field concrete, whether C-S-H will be formed at the early age during ASR period is much complicated and depends on the availability of Ca^{2+}. If the initial Ca^{2+} concentration in the pore solution is high enough, C-S-H can be found near the aggregate surface since ASR starts. However, the results of [69] also show that part of the initially formed C-S-H may uptake the available alkalis around and convert to a relative high-calcium ASR product. If the initial Ca^{2+} concentration in the pore solution is very low, no C-S-H but only low-calcium ASR products will be formed at the early age of ASR. Instead, the alkalis in these low calcium ASR products will exchange with

calcium and gradually convert to C-S-H after a couple of years or decades as reported by many researchers [6,73–75]. Unfortunately, this exchange effect is not implemented in the model yet due to the missing thermodynamic data. Another situation is that even if the initial Ca^{2+} is very low, if CH around the aggregate surface is abundant locally that it can buffer the Ca^{2+} to a local high concentration, C-S-H can also be formed near the aggregate surface.

3.3. The growth constant of KSH

Ten different values varying from 1.667×10^{-23} to $16.67\ m.\ s^{-1}$ for
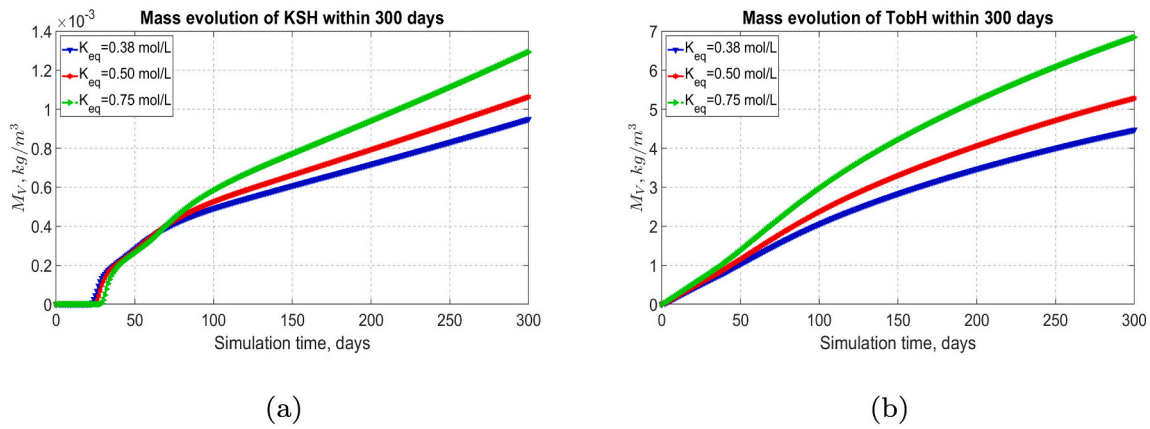
Fig. 5. The mass evolution represented by M_V of KSH and TobH in the domain with different alkali concentrations adopted in the cement paste and $\log K_5 = -8$ within 300 days. (**a**): The mass evolution of KSH; (**b**): The mass evolution of TobH.
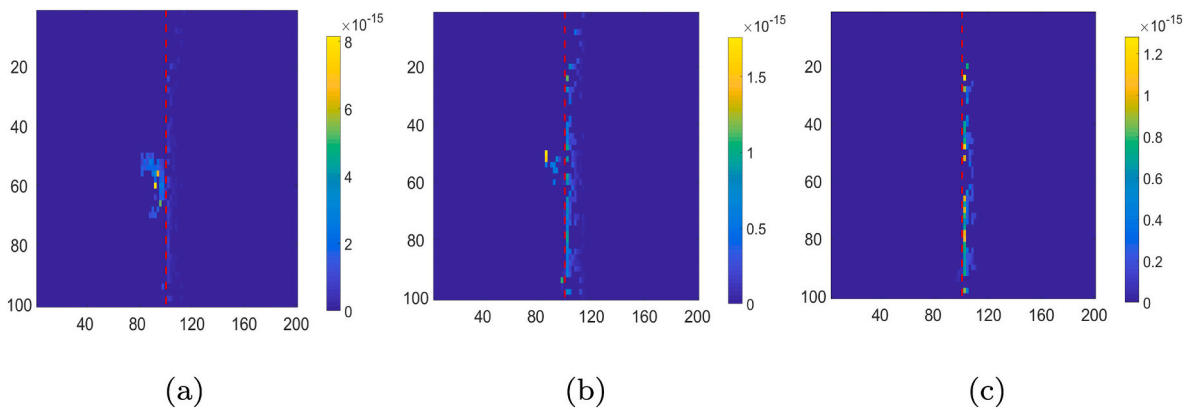

Fig. 6. Mass distribution of TobH on a random 2D slice when $\log K_5 = -10$ (**a**), $\log K_5 = -12$ (**b**), $\log K_5 = -14$ (**c**) within 270 days.

the growth constant K_g of KSH were studied to explore its influence on ASR. The input values were the same as those described in Section 3.2.1 except that K_5 was set to be 1×10^{-12}.

Fig. 7(a) shows the mass evolution of KSH in the domain with different K_g values used within 420 days. In the figure the curves with K_g varying from 1.667×10^{-11} $m \cdot s^{-1}$ to 16.67 $m \cdot s^{-1}$ are overlapping as well as the curves with K_g varying from 1.667×10^{-23} $m \cdot s^{-1}$ to 1.667×10^{-17} $m \cdot s^{-1}$. It can be seen that K_g has a great influence on the generated KSH. No KSH is formed as K_g is less than 1.667×10^{-14} $m \cdot s^{-1}$. When K_g is greater than 1.667×10^{-14} $m \cdot s^{-1}$, the generated KSH increases as K_g increases. But when K_g is equal to or greater than 1.667×10^{-11} $m \cdot s^{-1}$, the generated KSH does not change anymore with K_g increasing.

By comparing K_g with the maximum silica dissolution rate R_{SiO_2} in the model which is around 1.35×10^{-15} $m \cdot s^{-1}$ occurring at the beginning of the simulation when the OH^- was still high, it was found that KSH can only be numerously formed when K_g is greater than the silica dissolution rate. The greater K_g is, the faster KSH grows. When K_g is far greater (over 1000 times) than the silica dissolution rate, the growth of KSH is limited by the amount of the dissolved silica so that the produced KSH does not change anymore with K_g increasing. On the contrary, when K_g is less than the silica dissolution rate, no KSH is formed. The dissolved silica is consumed by the formation of TobH.

ASR kinetics has been reported either controlled by ion transport when highly reactive aggregate is used or by silica dissolution when slowly reactive aggregate is used (which is the situation in this section) [56]. However, a recent study [76] has numerically investigated a relative comprehensive sensitivity study about the effects of both of ion transport in aggregate and reactive mechanism (ASR gel production) on

ASR kinetics in a REV composed of cement paste and aggregate whose size varying from 2 to 125 mm. Their results have shown that the impact of reactive mechanisms on ASR kinetics is of prime importance, while the ion diffusion coefficients seem to have little effect when the temperature is higher than 10 °C. But no matter it is the ion transport or silica dissolution that controls the ASR kinetics, it is certain that a large value of K_g should be chosen to implement these two findings under different conditions.

In order to select a suitable value, we have also investigated if K_g has any influence on the location of KSH when it is larger than the silica dissolution rate. Fig. 7(b), (c) and (d) show the 3D mass distributions of KSH in the domain after 420 days with K_g varying from 1.667×10^{-7} m/s to 16.67 m/s. The Cartesian coordinates are shown in Fig. 7 (b). The 3D zone from $X = 0$ to $X = 100$ μm is the cement paste zone, while the 3D zone from $X = 101$ to $X = 200$ μm is the aggregate zone as also shown in Fig. 7(b). It is very obvious that K_g does not have a big influence on the location of KSH when it is over 1.667×10^{-14} m/s. Most of KSH is located inside the cement paste near the aggregate-cement paste interface after 420 days in all of systems. Based on the above analysis, a large value of 16.67 m/s is chosen for K_g in the model.

4. Application of the model

In literature, two fundamentally cracking patterns induced by ASR have been reported depending on the mineralogy of the aggregate. When the aggregate is highly reactive [77] or non-porous [78], silica dissolution takes place at the surface of the aggregate so that the initial expansion sites due to ASR gel formation develop and accumulate at the aggregate-cement paste interface which can crack the matrix around
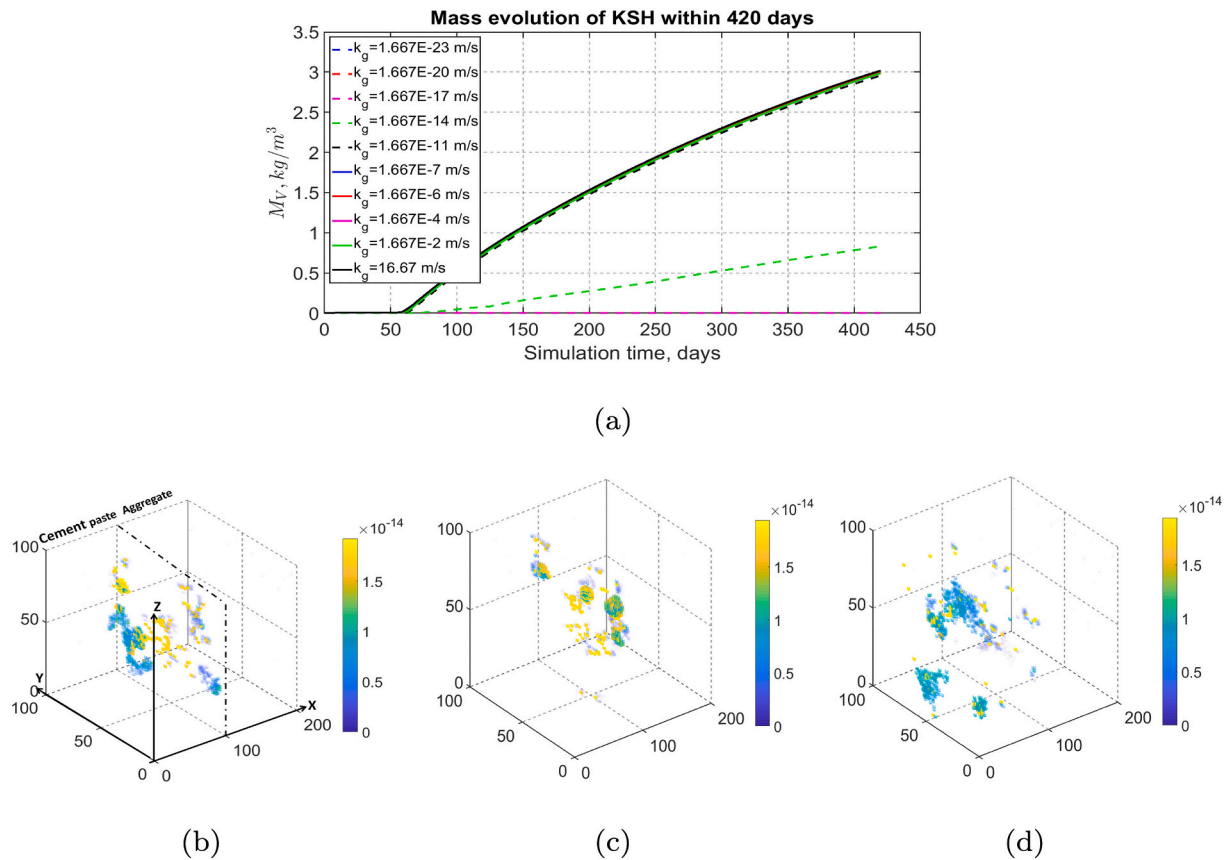
(a)

(b)   (c)   (d)

Fig. 7. (**a**): The mass evolution represented by M_V of KSH in the domain under different K_g within 420 days; 3D mass distribution of KSH in the domain after 420 days when $K_g = 1.667e - 7\ m/s$ (**b**), $K_g = 1.667e - 4\ m/s$ (**c**), $K_g = 16.67\ m/s$ (**d**). The unit of the color bar is *kg*.

[79]. A reaction rim around the aggregate surface can usually be found in this case [74]. When the aggregate is slowly reactive, the initial expansion sites develop in the aggregate leading to cracking from the inside of the aggregate and propagate to cement paste [77,78,80,81]. With respect to the crack pattern inside the aggregate, Sanchez et al. [78] further divided the cracking mechanism into two types: swelling of the bulk reactive aggregate due to the diffusion of alkali ions into the aggregate attacking the reactive silica; formation of veins full of ASR gel inside the reactive aggregate. Furthermore, they have also observed two typical cracks inside the aggregate: the 'sharp crack' which can pass through aggregates and the 'onion skin crack' which only propagates in the circumferential direction.

The earlier ASR simulation models only consider the ASR induced cracking in the cement paste and for the aggregate subjected to a compression pressure would not fracture [23,82,83]. New works have realized significant improvements on simulating different cracking patterns in the recent years. Based on the relationship between the quantitative void and crack content in the aggregate at microscopic and the mechanical measurements at macroscopic revealed by Haha et al. [81], Dunant and Scrivener [84] proposed a model that is able to predict the mechanical degradation of concrete induced by ASR cracking inside the aggregate. Both typical cracking patterns inside aggregate or in ITZ have been considered as a basis in the models of Iskhakov et al. [85] and Miura et al. [86]. In the work of Iskhakov et al. [85], the ASR induced microcrack growth in and around the aggregate is firstly modeled. The mechanical degradation at concrete level is then calculated. The model is able to provide a theoretical upper and lower range that characterizes the distribution of the gel in the aggregate or the cement paste for concrete degradation in experiments. In the work of Miura et al. [86], the crack pattern inside the aggregate is modelled as gel pocket randomly placed in the aggregate and the crack pattern in the ITZ is

modelled as a reaction rim surrounding the whole aggregate surface. Both 'sharp crack' and 'onion skin crack' were observed in their simulation.

Despite the improvement on considering different cracking patterns in the simulation models, the chemical mechanisms behind are ignored in these models. It is difficult to investigate the chemical mechanism behind these different crack patterns through experiment based on the fact that it can be affected by many factors such as alkali concentration, silica fraction, temperature etc. However, with the proposed model in this paper, it is possible to explore the chemical fundamentals behind these phenomenons by controlling part of the influential factors. In this section, we have applied the model using the determined parameters discussed above to investigate the influence of silica microstructural disorder degree on ASR by changing the dissolution rate of the silica. The reaction sequence, the expansion sites patterns which infers different cracking patterns as well as the mechanism behind when different reactive silica is used are discussed.

4.1. Input parameters

In this section, we have used the aggregate microstructure with a low silica fraction of 6.58%, which is more realistic in the field concrete, to form the initial domain. The other inputs were the same as those described in Section 3.3 except that the initial concentration of K_{eq}^+ was artificially increased to an average value of $0.75\ mol \cdot L^{-1}$ in order to provide enough alkalis. Two simulations with different dissolution rate were done. The change of the dissolution rate is realized by changing the activation energy E_a from 78,000 to 60000 $J \cdot mol^{-1}$. 78000 $J \cdot mol^{-1}$ represents that the silica is slow-reacting while 60000 $J \cdot mol^{-1}$ represents that the silica is rapid-reacting. The resulting silica dissolution rate had a difference of 3 orders of magnitude. The rapid-reaction system is

referred to the system A and the slow-reaction system is referred to the system B respectively in the continuation of the paper.

4.2. Investigation results

4.2.1. The formation sequence of ASR products

Firstly, the mass evolution represented by M_V of ASR products in both systems is shown in Fig. 8. The blue curve is obtained from system A while the red curve is from system B. Fig. 8(a), the mass evolution of KSH, shows that in system A when the silica dissolution rate is fast, much more KSH (18 kg/m^3 after 270 days) is formed than when the silica dissolution rate is slow (0.065 kg/m^3 after 270 days). KSH grows very fast in system A but its growth rate gradually decreases with time. However, in system B, KSH grows very slowly before around 240 days while the growth rate soars after 240 days. The mass evolution of TobH is different from that of KSH in the systems as can be seen from Fig. 8(b). At around 235 days, the mass of TobH in the two systems almost reaches the same value. TobH in system A grows very fast after the simulation starts and stops growing at around 60 days. In system B, TobH grows at a stable rate but much slower than in system A and it does not stop growing after 270 days.

The results indicate that in system B when the silica dissolution rate is slow, TobH is formed firstly and the dissolved silica is mainly consumed by TobH. The growth of KSH is very slow before a certain time. However, in system A when the dissolution rate is fast, both of KSH and TobH grow very fast from the beginning of the simulation. Fig. 9 shows the concentration change of each ASR related ion in system A and system B. The Y axis is the average ion concentration in the domain, which is the total moles of each ion divided by the total volume of the domain. The peak value of the blue curve in Fig. 9(d) indicates that the reason behind these different formation sequences is that $H_2SiO_4^{2-}$ needs to reach a threshold concentration to supersaturate the solution for KSH to be formed. Before the threshold level, no KSH is formed. When silica dissolution is fast, $H_2SiO_4^{2-}$ shoots up to a high level very soon then it decreases as KSH starts to be formed as indicated by the fast dropping of the K_{eq}^+ in Fig. 9(c). When silica dissolution is slow, it takes a longer time for the $H_2SiO_4^{2-}$ to reach the threshold concentration (around 240 days). However, the thermodynamic state of TobH is more sensitive to Ca^{2+} concentration. TobH is formed immediately when $H_2SiO_4^{2-}$ is released and the concentration of Ca^{2+} is high as can be seen from the dropping trend of Ca^{2+} in Fig. 9(a).

4.2.2. Location of ASR products

Fig. 10 shows the mass location evolution represented by $M_{V_{YOZ}}$ ($kg \cdot m^{-3}$) of KSH in the two systems within 270 days. Here, $M_{V_{YOZ}}$ is the normalized mass per cubic meter on each YOZ plane that equals to the mass of the formed phase on each YOZ plane divided by the total volume

of the domain. The X axis is the distance of the YOZ to the most left one where $X = 0$. In system A where the silica dissolution is rapid, KSH is only formed at the aggregate-cement paste zone after 1 day as indicated by the yellow curve in Fig. 10(a). But very soon, KSH is formed both at the aggregate-cement paste zone and in the cement paste with most of KSH formed in the cement paste. In system B where the silica is less reactive and the dissolution is slow, KSH is generated inside the aggregate with a distance more than 20 μm before 270 days. After 270 days, KSH is also found in the cement paste as shown by the blue curve in Fig. 10(b).

Let's have a look at the ion concentration evolution again in Fig. 9. In system A when the silica dissolution is fast, OH^- plunges to a stable level very quickly after the simulation starts as shown by the blue curve in Fig. 9(b). Most of OH^- is consumed by the dissolution of the reactive silica as illustrated by the blue curve in Fig. 9(d) showing that the concentration of $H_2SiO_4^{2-}$ increases at the same time as OH^- decreases. Due to the fast dissolution, most of OH^- is consumed very quickly near the surface of the aggregate. This is confirmed in Fig. 11(a). Just after 3 days (red curve in Fig. 11(a)), the concentration of OH^- is reduced by half and the diffusion distance (around 30 μm) in the aggregate does not change a lot compared to that after one day (blue curve in Fig. 11(a)). After 30 days (rose red curve in Fig. 11(a)), OH^- is consumed to such a level that its diffusion distance in the aggregate decreases to only few micrometers. As a consequence, the dissolution sites only locate near the surface of the aggregate and the dissolved $H_2SiO_4^{2-}$ is firstly mainly concentrated in the dissolution sites as shown in Fig. 11(c). After one day (blue curve in Fig. 11(c)), $H_2SiO_4^{2-}$ is mainly found in the aggregate within a distance of around 30 μm. A small part of $H_2SiO_4^{2-}$ is able to diffuse into the cement paste. This is why KSH mainly formed in the aggregate-cement paste zone in system A in the beginning of the simulation. With simulation going, more silica in the aggregate-cement paste zone is dissolved resulting that the porosity there is increased which makes it more easily for $H_2SiO_4^{2-}$ in the aggregate to diffuse out into the cement paste plus that the dissolved $H_2SiO_4^{2-}$ locates very near the aggregate-cement paste zone. After 3 days (red curve in Fig. 11(c)), more $H_2SiO_4^{2-}$ is diffused into the cement paste but the concentration in the aggregate-cement paste zone is still very high. Nevertheless, after 12 days and 30 days (green and rose red curves in Fig. 11(c)), the concentration of $H_2SiO_4^{2-}$ in the cement paste exceeds that in the aggregate. The high concentration of $H_2SiO_4^{2-}$ makes the solution more easily to be supersaturated for KSH in the cement paste than that in the aggregate since the concentration of K_{eq}^+ in the cement paste is higher than that in the aggregate due to low permeability of the aggregate. As a result, KSH starts to be formed in the cement paste.

In system B, due to the slow dissolution of silica, the concentration of OH^- is kept at a high level within a long period so that it can diffuse into the aggregate in a long distance as shown in Fig. 11(b). After one day
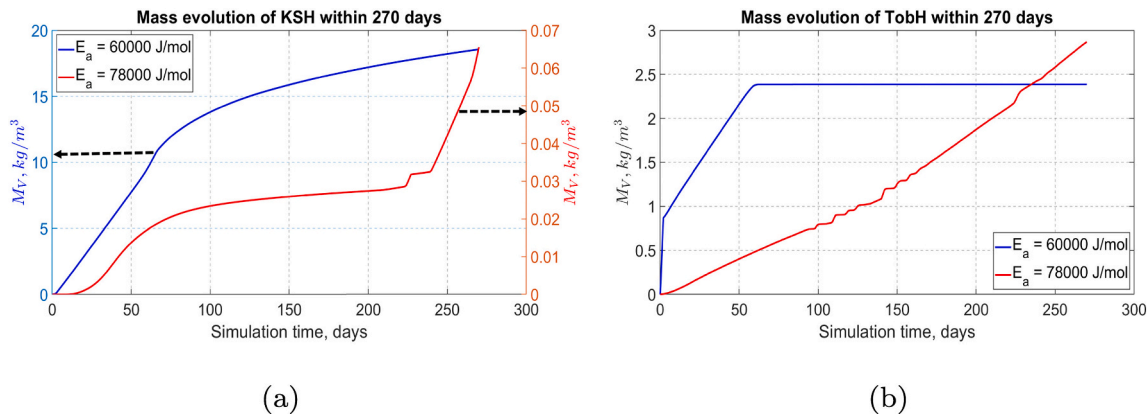

Fig. 8. The mass evolution represented by M_V of ASR products in system A and system B within 270 days. (**a**): The mass evolution of KSH; (**b**): The mass evolution of TobH.
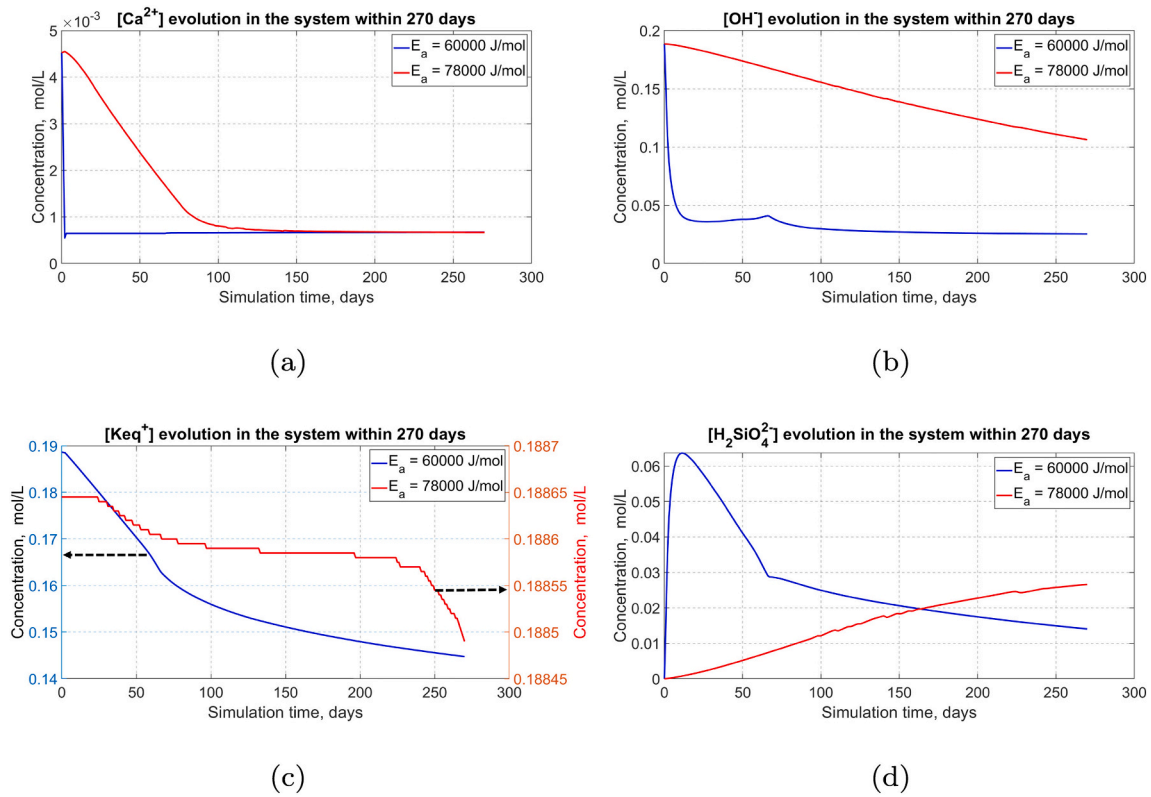
(a)

(b)

(c)

(d)

Fig. 9. Comparison of the ion concentration evolution between system A and system B within 270 days. (**a**): The change of $[Ca^{2+}]$; (**b**): The change of $[OH^-]$; (**c**): The change of $[K_{eq}^+]$; (**d**): The change of $[H_2SiO_4^{2-}]$; The concentration of each ion is the total moles of each ion divided by the total volume of the domain, which is 1×10^{-12} m^3.
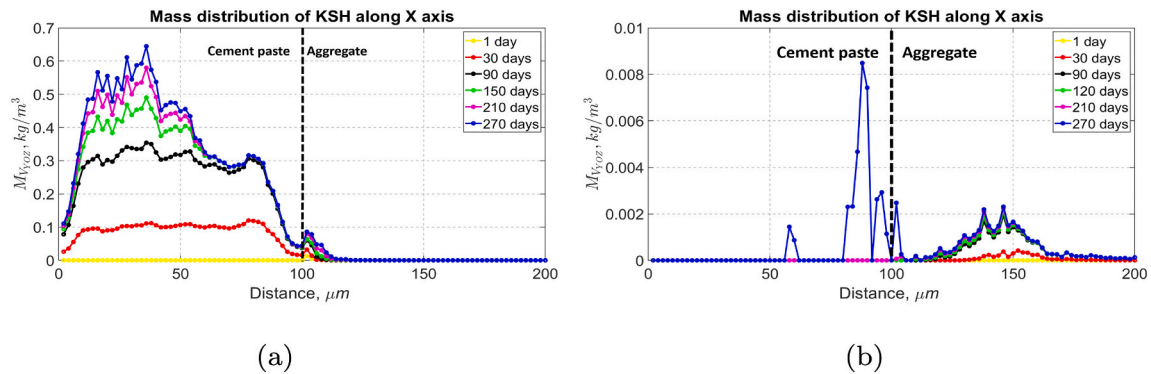

(a)

(b)

Fig. 10. The location evolution of KSH with time in system A system B within 270 days. (**a**): In system A with $E_a = 60000$ $J \cdot mol^{-1}$; (**b**): In system B with $E_a = 78000$ $J \cdot mol^{-1}$.

(blue curve in Fig. 11(b)), OH$^-$ diffuses into a distance of around 40 μm in the aggregate and after 30 days (red curve in Fig. 11(b)), it is able to diffuse into the whole aggregate domain. At the same time the silica is dissolved in a slow rate where OH$^-$ is present, the concentration of H$_2$SiO$_4^{2-}$ is much lower than that in system A as shown in Fig. 11(d). After 30 days (red curve in Fig. 11(d)), the maximum concentration of H$_2$SiO$_4^{2-}$ in system B is around 0.08 $mol \cdot L^{-1}$, while it reaches around 0.23 $mol \cdot L^{-1}$ in system A just after one day. Furthermore, the slow dissolution of silica does not change the porosity of the aggregate a lot in a long term. As a result, it is more difficult for H$_2$SiO$_4^{2-}$ to diffuse out and KSH is mainly formed inside the aggregate in a long period. However, as long as the simulation time is long enough, it is possible for H$_2$SiO$_4^{2-}$ to reach the threshold level in the cement paste for KSH to be formed.

Fig. 12 shows two random slices of TobH mass distribution from

system A and system B. In system A, TobH is mainly formed inside the cement paste as shown by Fig. 12(a) due to the fast release and fast diffusion of H$_2$SiO$_4^{2-}$ into the cement paste. In system B, the release of H$_2$SiO$_4^{2-}$ is slow and is accumulated inside the aggregate so that TobH is formed inside the aggregate within a short distance to the interfacial surface (around 20 μm) where Ca^{2+} can diffuse into as shown by Fig. 12 (b).

4.2.3. Spatial correlation between KSH and aggregate microstructure

We have discussed in the last section about the location evolution of ASR products both in system A and B and its corresponding mechanisms. KSH is found in the aggregate in both systems. In this section, the location of initial reactive silica zone, the remaining reactive silica after a target simulation time and the KSH on some 2D slices extracted from the inside of the aggregate will be presented to show the spatial
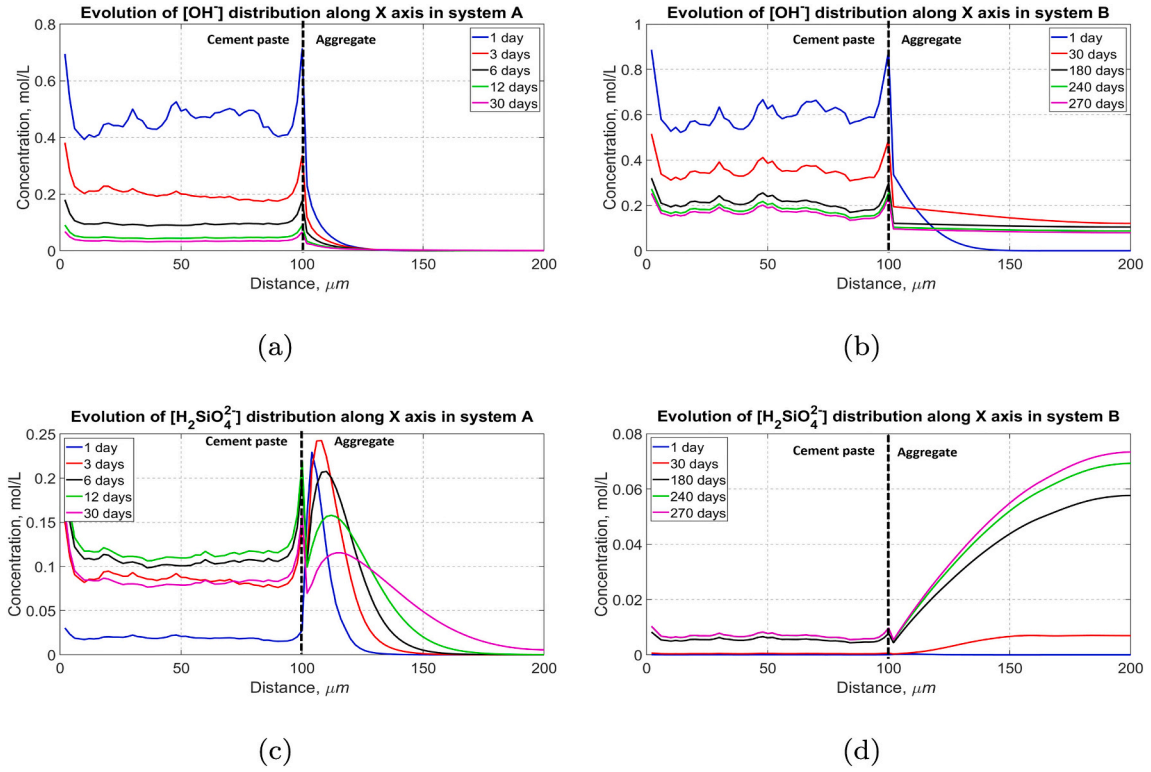
(a)

(b)

(c)

(d)

Fig. 11. Evolution of the average concentration distribution of OH⁻ and H₂SiO₄²⁻ on the YOZ plane along *X* axis in system A and system B. (**a**): [OH⁻] in system A within 30 days; (**b**): [OH⁻] in system B within 270 days; (**c**): [H₂SiO₄²⁻] in system A within 30 days; (**d**): [H₂SiO₄²⁻] in system B within 270 days. The yellow dashed line distinguishes the cement paste zone and the aggregate zone. (For interpretation of the references to color in this figure legend, the reader is referred to the web version of this article.)
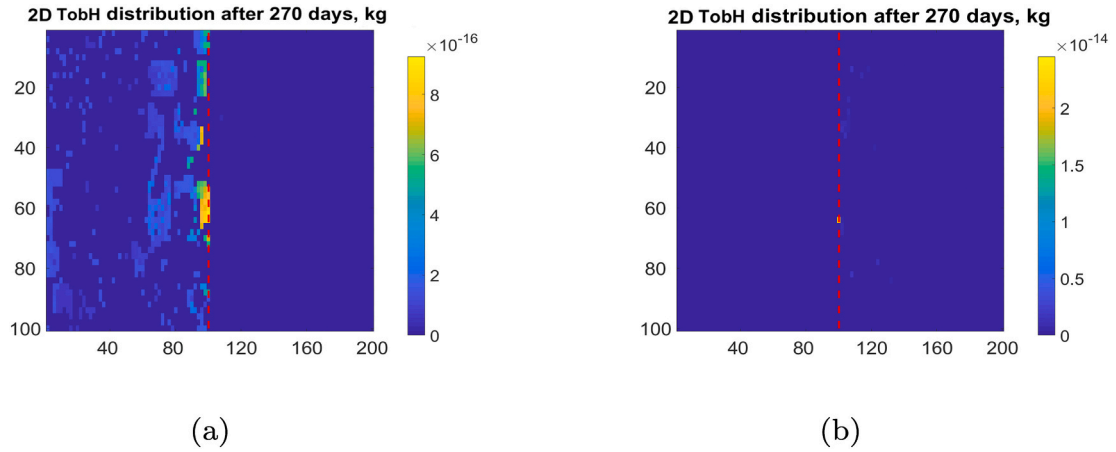

(a)

(b)

Fig. 12. Random 2D mass distribution slice of TobH from system A (**a**) and system B (**b**) within 270 days.

correlation between KSH and the aggregate microstructure in both system A and system B.

Fig. 13 (a), (b) and (c) show the mass distribution of the initial reactive silica zone in the aggregate used in the model at a distance to the aggregate-cement paste interface of 2 μm, 6 μm and 10 μm respectively. The navy blue part is the reactive silica while the yellow part is other minerals in the aggregate. Every node is full of solid and for the silica node, its mass is 2.04×10^{-14} *kg* per node. Fig. 13 (d), (e) and (f) show the mass distribution of the reactive silica on Fig. 13 (a), (b) and (c) after simulation of 60 days in system A respectively. It can be seen that after 60 days, at a distance of 2 μm, all of the reactive silica on the slice is dissolved. At a distance of 6 μm, only a small part of the reactive silica remains, while at a distance of 10 μm, only a small part of silica is

dissolved. Fig. 13 (g), (h) and (i) show that in the aggregate, KSH is formed at where the silica is dissolved and with the distance to the aggregate-cement interface increasing, less KSH is formed. In another word, the reactive silica zone is surrounded by a KSH rim. With time going, the KSH rim gets thicker while the reactive silica zone is attacked deeper.

In system B where the silica dissolution is slow, KSH is formed inside the aggregate with a relatively far distance as shown by Fig. 10(b). Fig. 14 (a), (b), (c) show the initial mass distribution of the initial reactive silica zone in the aggregate at a distance to the aggregate-cement interface of 40 μm, 46 μm and 50 μm respectively. Fig. 14 (d), (e) and (f) show the mass distribution of the reactive silica on Fig. 14 (a), (b) and (c) after simulation of 360 days in system B respectively. It can
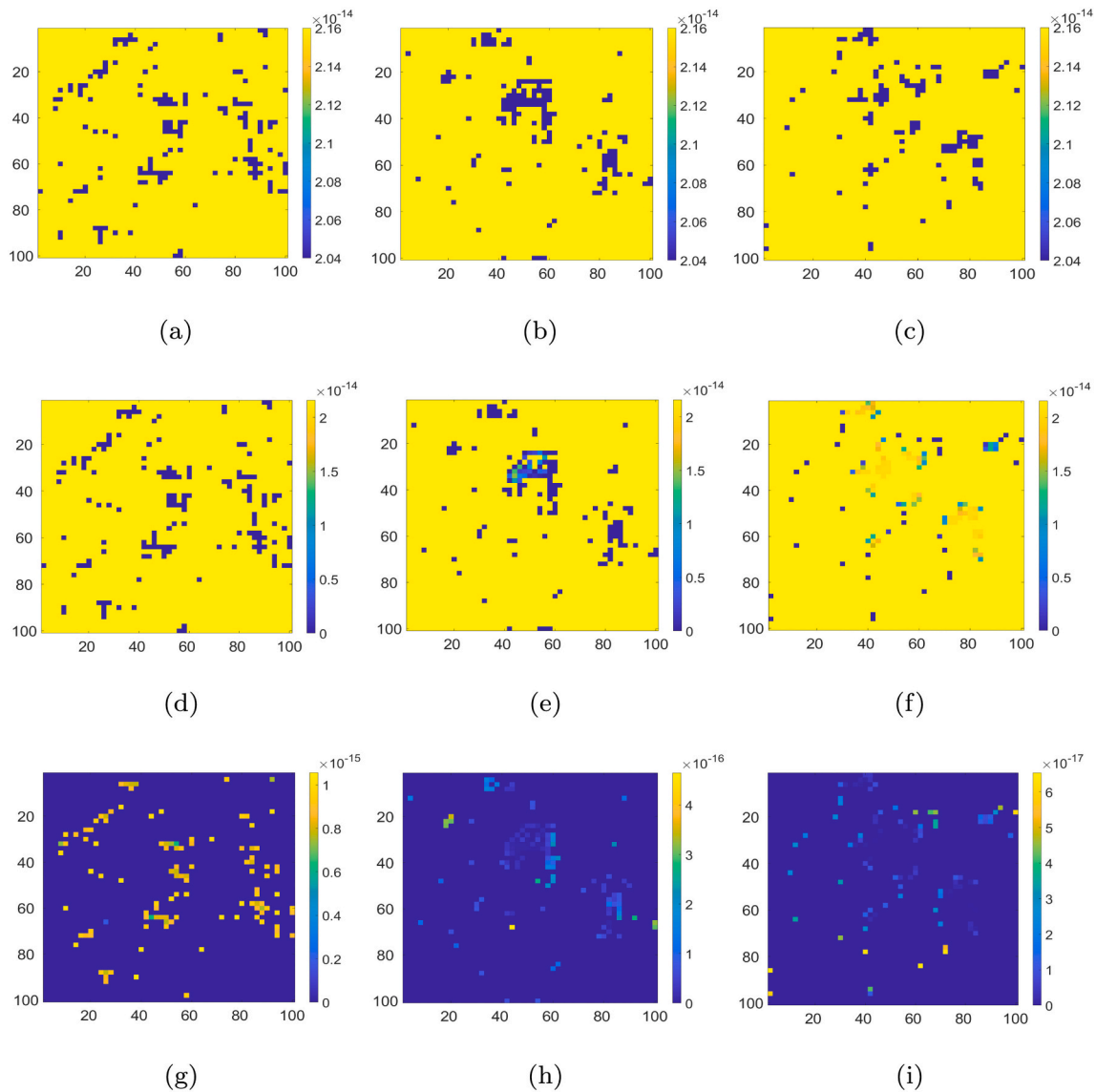
Fig. 13. (a), (b), (c): The mass distribution of initial reactive silica zone in the aggregate at a distance to the aggregate-cement interface of 2 μm, 6 μm and 10 μm respectively. The navy blue part is reactive silica and the yellow part is other minerals in the aggregate; **(d), (e), (f)**: The mass distribution of the remain reactive silica on slice (a), (b), (c) respectively after 60 days in system A respectively. The yellow part is other minerals in the aggregate, while the other colors represents reactive silica with different mass in a node; **(g), (h), (i)**: The mass distribution of the formed KSH on slice (a), (b), (c) after 60 days in system A respectively. The unit scales of the figures and color bars are μm and kg respectively.

be seen that after 360 days, the dissolved silica on each slice is almost identical to each other, which confirms that the diffusion of ions in the aggregate can reach a far distance than in system A. Again, KSH is formed where silica is dissolved as shown by Fig. 14 (g), (h) and (i).

In general, most of KSH is formed at where silica is dissolved inside the aggregate. When the silica dissolves fast, the model is able to simulate a KSH rim around the reactive silica zone in the aggregate near to the aggregate-cement paste interface as most of ions are consumed there. When the silica dissolves slowly, KSH is formed inside the reactive silica zone at where silica is dissolved as ions are not reduced greatly and can diffuse further in the aggregate. The above results also indicate that rate-controlling step is the dissolution of the silica in the above two systems even if the MIP porosity of the aggregate is as small as 0.8%.

5. Discussion

5.1. The impact of the equilibrium constant and the growth rate of KSH

The sensitivity analysis has shown that the equilibrium constant of KSH K_5 has a great influence on the formed ASR products. Either TobH or KSH is not formed when K_5 is too small or too large. Furthermore, K_5 also affects the location of TobH. TobH is easier to be found in the cement paste when K_5 is large. A suitable value of 1×10^{-12} for the equilibrium constant of KSH K_5 is chosen in the model so that both TobH and KSH can be formed and the location of TobH is concentrated near the aggregate-cement paste interface. This value is less than that of the crystal KSH synthesized under 40^oC, which is about 1×10^{-8} [47]. This is reasonable bearing in mind that KSH in the model is assumed to be amorphous. In general, non-crystalline phases have a higher solubility than their crystalline compositional equivalents. In available ASR thermodynamic models [39,41,87], magadiite, okenite and kanemite have been used as surrogates for low Ca/Si ASR gel based on their similarities
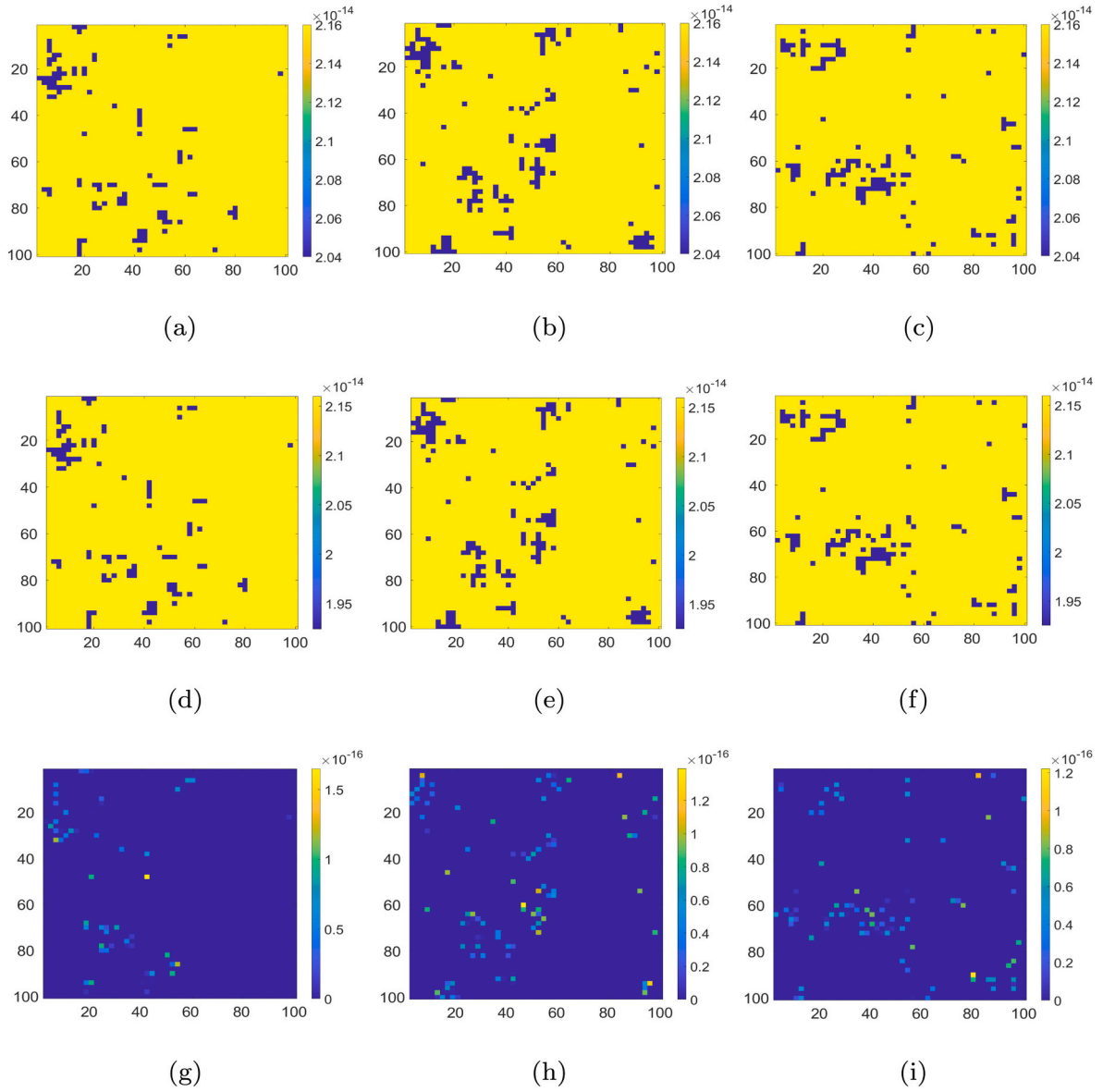
Fig. 14. (a), (b), (c): The mass distribution of initial reactive silica zone in the aggregate at a distance to the aggregate-cement interface of 40 *μm*, 46 *μm* and 50 *μm* respectively. The navy blue part is reactive silica and the yellow part is other minerals in the aggregate; **(d), (e), (f):** The mass distribution of the remain reactive silica on slice (a), (b), (c) respectively after 360 days in system B. The yellow part is other minerals in the aggregate, while the other colors represents reactive silica with different mass in a node; **(g), (h), (i):** The mass distribution of the formed KSH on slice (a), (b), (c) respectively after 360 days in system B. The unit scales of the figures and color bars are *μm* and *kg* respectively.

in composition. We have recalculated their equilibrium constants based on the thermodynamic data in [39,41] with H_2SiO_4 or $SiO_2(aq)$ and H^+ transferred to the used ion $H_2SiO_4^{2-}$ and OH^- in this paper. The calculated equilibrium constants are 1×10^{-3}, 1×10^{-18} and 1 for magadiite, okenite and kanemite respectively. Obviously, these equilibrium data are either too big or too small compared with the determined value in this paper. Based on our sensitivity analysis results, the generated ASR products in these models would be overestimated or underestimated since tobermorite was also considered in these models. It needs to be noticed that the determined value in this paper is only suitable under 25^oC. For a higher temperature, the value should be less than 1×10^{-12} considering KSH is more easy to dissolve at a high temperature [47].

Sensitivity analysis also indicates that the growth constant of KSH K_g does not have a big influence on ASR, such as the reaction degree evolution, the mass evolution of KSH as well as its location as long as K_g is greater (at least 100 times in this paper) than the silica dissolution rate.

In literature, the kinetics of ASR has also been reported to be controlled either by silica dissolution or ion diffusion depending on the reactive silica polymorphs contained in the aggregate the aggregate [56,76]. In this model, a large value of 16.67 *m/s* for K_g is chosen. This value should be large enough to guarantee the silica dissolution or ion diffusion as the rate-limit step for simulation with any reactive silica polymorphs.

5.2. The impact of silica microstructural disorder degree

We have implemented two different silica dissolution rates in the model to investigate the influence of the silica microstructural disorder degree on ASR. The classic distributions of the expansion sites in the concrete with rapid-reacting and slowly-reacting aggregate [77] are simulated successfully in the simulations. In the system with the fast dissolving silica, ASR products are located in the aggregate-cement paste zone in the beginning but very soon KSH is formed all over in the cement paste. This is corresponding to the findings in [77] that a reaction rim of

about 1 *mm* was found in the concrete with rapid-reacting aggregate. In [74], a reaction rim is also formed around the glass bead embedded in an alkaline solution. In the system with slowly dissolving silica, the expansion sites are located inside the aggregate in a long-term. Leemann et al. [44] have also confirmed this location pattern in slowly-reactive aggregate by adding caesium to concrete to trace the reaction sequence of ASR. One difference in our simulation is that after 270 days KSH is also found in the cement paste. This may attribute to the different environment conditions and testing time in [44,77]. Both field concrete and laboratory test samples were used in [77], the solution environment as well as the testing time were not clear in these samples. The testing time in [44] was around 20 weeks, which probably was not long enough for ASR products to be formed in the cement paste. On the other hand, the following induced crack is not simulated and coupled in this model. Thus, it is also possible that KSH is formed inside the ASR-induced cracks inside the aggregate rather than in cement paste in field concrete.

A possible mechanism for the two different patterns is also provided by the model. When the silica dissolves fast, OH^- is consumed quickly in the aggregate-cement paste zone enabling the dissolved silica to diffuse into the cement paste very easily. Meanwhile, the low concentration of OH^- makes it is unable to diffuse into the aggregate further. As a result, ASR products are formed at the aggregate-cement paste zone and in the cement paste. While when the silica dissolves slowly, OH^- is consumed in a slow rate and is able to diffuse into the aggregate so that the reaction front is distributed all over the inside of the aggregate. The low permeability of the aggregate makes it difficult for the dissolved $H_2SiO_4^{2-}$ to diffuse out. Consequently, ASR products are formed inside the aggregate. But with time on going, the dissolved $H_2SiO_4^{2-}$ in the cement paste can also reach a threshold level for KSH to be formed there.

Besides, the simulation results also reveal two different formation sequences of ASR products. When silica dissolves very fast, both TobH and KSH are formed very soon after the simulation starts. However, when silica dissolves slowly, TobH is formed firstly and KSH is not formed until around 240 days. The second sequence is also proposed by Kim et al. [39] and Leemann et al. [88]. They have investigated the solid and the solution change in a simple chemical systems composed by the slow-reacting cristobalite (in [39]) or micro silica (in [88]) and alkaline solution. Their results showed that ASR gel was not generated until the calcium hydroxide was consumed to a low level by the formation of C-S-H and the concentration of the dissolved silica was accumulated to a level. This is corresponding to the finding proposed before that there is a threshold concentration of $H_2SiO_4^{2-}$ for KSH to be formed.

The proposed model in this paper is able to trace the entire chemical reaction process of ASR between the cement paste and the aggregate at microscale. Not only can the quantitative data such as mass, extra volume produced and reaction degree evolution obtained, but also qualitative information such as the distribution of ASR products and ions. Possible mechanisms can be provided by the model for some discovered phenomenon in the field or in the laboratory. However, there are some discrepancies between the real situation and the simulation. According to a recent study [89], the porosity of ASR products can be as high as 80%, which means that its expansion ratio may be different from the one used in the model (0.5), thus the subsequent induced strain can be different. This discrepancy can be resolved by resetting the density of ASR products in the model before the simulation.

The 3D microstructure of the limestone in this work is simulated using the correlation functions based on its 2D SEM-BSE microstructure images as elaborated in our former paper [30]. Unfortunately, due to the computer resources limitation, the pore size below 1 μm is not kept. The final simulated 3D microstructure contains the real distribution of reactive silica, non-reactive materials and air void (size above the simulation resolution which is 1 μm) whose fraction is too small that can be ignored. In order to compensate this loss, homogeneous ions diffusion coefficients are applied in the aggregate based on the MIP detected porosity. This is different from that in field concrete. It has been shown that initial ASR products form dominantly in the pre-existing cracks and

reactive silica zone boundaries in the siliceous aggregates [44,75]. Theoretically, the reaction in the pre-existing cracks can also be simulated using the present model, as long as the size of the pre-existing cracks is larger than $1\mu m$ so that it can be captured in the final 3D microstructure using the method in [30]. On the other hand, the reaction fronts in the model contains not only the reactive silica zone boundaries but also inside the reactive silica zone since we assume that ions can diffuse through the silica resulting ASR products being formed both around grain boundaries (when silica dissolves fast) and inside the silica grain (when silica dissolves slowly). This part can be further improved in future by constraining the permeable phases in the aggregate where the ions can diffuse through.

Another limitation of the model is that the aggregate microstructure size at microscale is limited by the computer resources. In this paper, we adopted a size of 100 × 100 × 100 μm. It needs more computation resource and a longer simulation time as the size increases. As a result, assumptions are needed to calculate the mass of ASR products in aggregate relatively further than 100 μm if one tries to simulate the induced mechanical degradation at a higher scale.

Furthermore, the present model focus on simulating ASR in the early stage, and no following cracking is considered yet. Our future work will simulate the different initial cracking mechanisms induced by the initial products at different locations. Once cracking, ions will be able to diffuse into the aggregate more easily and the location of ASR products will change too. This part needs a coupling work of cracking and chemical reaction simulation in a model at the same time, which is more realistic but more difficult. The future of ASR modeling will probably see such a combination.

6. Conclusion and perspectives

In this paper an innovative 3D reactive transport model at microscale is proposed. By coupling ion diffusion, the model permits a detailed characterization of the chemical reaction process of ASR including silica dissolution, dissolution of CH and C-S-H, nucleation and growth of ASR products when cement paste is in touched with aggregate.

The details about the methodologies to implement these different reaction processes and the ion diffusion are firstly stated. Important parameters are then calibrated. After that, the model is applied to two systems with different silica dissolution rate to investigate the influence of silica microstructural disorder degree on ASR. The following remarks can be made.

(1) The adoption of the equilibrium constant of KSH K_5 in a simulation model plays an important role on the formed type of ASR products as well as on the location of the formed TobH. When K_5 is too small, only KSH is formed and when it is too large, only TobH is formed. TobH tends to be formed in the cement paste with K_5 increasing. A middle value of 1×10^{-12} is chosen in the present model.

(2) In order to make sure the rate-control step of ASR is the silica dissolution or ions transport, a big value for the growth constant of KSH K_g should be chosen in a simulation model. When K_g is less than the silica dissolution rate, no KSH is formed. The dissolved silica is consumed by the formation of TobH. When K_g is greater than the silica dissolution rate, the amount of KSH firstly increases with increasing K_g, but when K_g is far greater than the silica dissolution rate (100 times in this paper), it does not affect the amount of KSH as well as its location anymore. A value of 16.67 $m \cdot s^{-1}$ is chosen in the present model.

(3) By adopting the MRT method to simulate ion diffusion, the influence of the relaxation time τ on the ion diffusion is greatly decreased so that a relatively large τ (1200 in this work) can be adopted to decrease the number of iterations while not sacrificing the ion diffusion accuracy.

(4) Using the calibrated parameters with other fixed thermodynamic and kinetic parameters, the model is able to simulate the two typical expansion sites patterns found in field concrete and in laboratory experiments. Expansive sites are located in the aggregate-cement paste zone when the aggregate is highly reactive or inside the aggregate when the aggregate is less reactive. A possible mechanism is provided by the model behind these two patterns based on the simulated ions evolution and ions distribution in the domain. In addition, it is discovered by the model that the formation sequence of ASR products is different when the silica dissolution rate is different. Given the initial Ca^{2+} concentrtaion is high, when the silica is highly reactive, both of TobH and KSH are formed very soon, while when the silica is less reactive, TobH is formed firstly and KSH is not formed until the concentration of $H_2SiO_4^{2-}$ reaches a threshold level.

The proposed model can be extended to simulate the influence of other factors on ASR such as alkali concentration, temperature and permeability of the aggregate. It is possible to obtain a full picture about the ASR reaction mechanism in the eary stage using the model. On the other hand, the output of the mass distribution of KSH can be used to calculate the local stress inside the domain which can be used as inputs in a lattice cracking model [90] to simulate the initial cracking at a larger scale. As such, the initial cracking development at large scale is captured without sacrificing or simplifying the chemical fundamentals at microscale.

CRediT authorship contribution statement

Xiujiao Qiu: Conceptualization, Methodology, Software, Validation, Formal analysis, Investigation, Data curation, Writing – original draft, Visualization. **Jiayi Chen:** Software, Methodology. **Guang Ye:** Resources, Supervision. **Geert De Schutter:** Resources, Supervision, Project administration, Writing – review & editing, Funding acquisition.

Declaration of competing interest

The authors declare that they have no known competing financial interests or personal relationships that could have appeared to influence the work reported in this paper.

References

[1] L.D. Glasser, N. Kataoka, The chemistry of 'alkali-aggregate' reaction, Cem. Concr. Res. 11 (1981) 1–9.

[2] J.D. Rimstidt, Rate equations for sodium catalyzed quartz dissolution, Geochim. Cosmochim. Acta 167 (2015) 195–204.

[3] T.C. Powers, H.H. Steinour, An interpretation of some published researches on the alkali-aggregate reaction Part 1-the chemical reactions and mechanism of expansion, in: J. Proc. 51 (1955) 497–516.

[4] L.J. Struble, S. Diamond, Swelling properties of synthetic alkali silica gels, J. Am. Ceram. Soc. 64 (1981) 652–655.

[5] W. Wieker, C. Hubert, D. Heidemann, R. Ebert, M. Bérubé, B. Fournier, B. Durand, Some experiences in chemical modelling of the alkali-silica reaction, in: 11th International Conference on Alkali-aggregate Reactions, Quebec, 2000, pp. 119–128.

[6] M. Brouxel, The alkali-aggregate reaction rim: Na2O, SiO2, K2O and CaO chemical distribution, Cem. Concr. Res. 23 (1993) 309–320.

[7] P. Rivard, J.P. Ollivier, G. Ballivy, Characterization of the ASR rim: application to the Potsdam sandstone, Cem. Concr. Res. 32 (2002) 1259–1267.

[8] C. Larive, Apports combinés de l'expérimentation et de la modélisation à la compréhension de l'alcali-réaction et de ses effets mécaniques, Ecole nationale des ponts et chaussees, 1997. Ph.D. thesis.

[9] I. Comby Peyrot, F. Bernard, P.O. Bouchard, F. Bay, E. Garcia-Diaz, Development and validation of a 3D computational tool to describe concrete behaviour at mesoscale. Application to the alkali-silica reaction, Comput. Mater. Sci. 46 (2009) 1163–1177.

[10] C. Comi, R. Fedele, U. Perego, A chemo-thermo-damage model for the analysis of concrete dams affected by alkali-silica reaction, Mech. Mater. 41 (2009) 210–230.

[11] V. Saouma, L. Perotti, Constitutive model for alkali-aggregate reactions, ACI Mater. J. 103 (2006) 194.

[12] R. Esposito, M. Hendriks, Literature review of modelling approaches for ASR in concrete: a new perspective, Eur. J. Environ. Civ. Eng. 23 (2019) 1311–1331.

[13] Z.P. Bažant, G. Zi, C. Meyer, Fracture mechanics of ASR in concretes with waste glass particles of different sizes, J. Eng. Mech. 126 (2000) 226–232.

[14] L. Dormieux, E. Lemarchand, D. Kondo, E. Fairbairn, Elements of poro-micromechanics applied to concrete, Mater. Struct. 37 (2004) 31–42.

[15] R. Esposito, M.A. Hendriks, A multiscale micromechanical approach to model the deteriorating impact of alkali-silica reaction on concrete, Cem. Concr. Compos. 70 (2016) 139–152.

[16] T. Wu, I. Temizer, P. Wriggers, Multiscale hydro-thermo-chemo-mechanical coupling: application to alkali–silica reaction, Comput. Mater. Sci. 84 (2014) 381–395.

[17] H. Schlangen, O. Copuroglu, Modeling of expansion and cracking due to ASR with a 3D lattice model, in: FraMCos-7: Proceedings of the 7th International Conference on Fracture Mechanics of Concrete and Concrete Structures, Jeju Island, Korea, 2010, 23-28 May.

[18] E. Lemarchand, L. Dormieux, F.-J. Ulm, Micromechanics Investigation of Expansive, 2005.

[19] L. Charpin, Modèle micromécanique pour l'étude de l'anisotropie de la réaction alcali-silice, Ph.D. thesis, Université Paris-Est, 2013.

[20] L. Charpin, A. Ehrlacher, Microporomechanics study of anisotropy of ASR under loading, Cem. Concr. Res. 63 (2014) 143–157.

[21] É. Grimal, A. Sellier, Y. Le Pape, É. Bourdarot, Creep, shrinkage, and anisotropic damage in alkali-aggregate reaction swelling mechanism-part I: a constitutive model, ACI Mater. J. 105 (2008) 227.

[22] É. Grimal, A. Sellier, Y. Le Pape, É. Bourdarot, Creep, shrinkage, and anisotropic damage in alkali-aggregate reaction swelling mechanism-part II: identification of model parameters and application, ACI Mater. J. 105 (2008) 236.

[23] Z.P. Bažant, A. Steffens, Mathematical model for kinetics of alkali–silica reaction in concrete, Cem. Concr. Res. 30 (2000) 419–428.

[24] W. Puatatsananon, V. Saouma, Chemo-mechanical micromodel for alkali-silica reaction, ACI Mater. J. 110 (2013) 67.

[25] V.E. Saouma, R.A. Martin, M.A. Hariri-Ardebili, T. Katayama, A mathematical model for the kinetics of the alkali–silica chemical reaction, Cem. Concr. Res. 68 (2015) 184–195.

[26] S. Multon, A. Sellier, Multi-scale analysis of alkali–silica reaction (ASR): impact of alkali leaching on scale effects affecting expansion tests, Cem. Concr. Res. 81 (2016) 122–133.

[27] Z.P. Bažant, S. Rahimi-Aghdam, Diffusion-controlled and creep-mitigated ASR damage via microplane model. I: mass concrete, J. Eng. Mech. 143 (2017) 04016108.

[28] M. Nguyen, J. Timothy, G. Meschke, Numerical analysis of multiple ion species diffusion and alkali-silica reaction in concrete, in: Computational Modelling of Concrete Structures (EURO-C), CRC Press, Taylor & Francis Group, St Anton am Alberg, 2014.

[29] S. Poyet, A. Sellier, B. Capra, G. Foray, J.M. Torrenti, H. Cognon, E. Bourdarot, Chemical modelling of alkali silica reaction: influence of the reactive aggregate size distribution, Mater. Struct. 40 (2007) 229.

[30] X. Qiu, J. Chen, M. Deprez, V. Cnudde, G. Ye, G.D. Schutter, 3D microstructure simulation of reactive aggregate in concrete from 2D images as the basis for ASR simulation, Materials 14 (2021) 2908.

[31] J. Chen, G. Ye, A lattice boltzmann single component model for simulation of the autogenous self-healing caused by further hydration in cementitious material at mesoscale, Cem. Concr. Res. 123 (2019), 105782.

[32] R. Helmuth, D. Stark, S. Diamond, M. Moranville-Regourd, Alkali-silica reactivity: an overview of research, Contract 100 (1993) 202.

[33] S. Girimaji, Lattice Boltzmann Method: Fundamentals and Engineering Applications With Computer Codes, AIAA, 2013.

[34] Z. Chai, Z. Huang, B. Shi, Z. Guo, A comparative study on the lattice boltzmann models for predicting effective diffusivity of porous media, Int. J. Heat Mass Transf. 98 (2016) 687–696.

[35] D. d'Humieres, Multiple–relaxation–time lattice boltzmann models in three dimensions, Philos. Trans. A Math. Phys. Eng. Sci. 360 (2002) 437–451.

[36] M. Mihara, R. Sasaki, Radio-nuclides Migration Datasets (RAMDA) on Cement, Bentonite and Rock for the Performance Assessment of TRU Waste Repository in Japan, Technical Report, Japan Nuclear Cycle Development Inst, 2005.

[37] R. Mills, V.M. Lobo, Self-diffusion in Electrolyte Solutions: A Critical Examination of Data Compiled From the Literature, Elsevier, 2013.

[38] F. Rajabipour, E. Giannini, C. Dunant, J.H. Ideker, M.D. Thomas, Alkali–silica reaction: current understanding of the reaction mechanisms and the knowledge gaps, Cem. Concr. Res. 76 (2015) 130–146.

[39] T. Kim, J. Olek, Chemical sequence and kinetics of alkali–silica reaction part II. A thermodynamic model, J. Am. Ceram. Soc. 97 (2014) 2204–2212.

[40] H. Wang, J. Gillott, Mechanism of alkali-silica reaction and the significance of calcium hydroxide, Cem. Concr. Res. 21 (1991) 647–654.

[41] G.D. Guthrie, J.W. Carey, A thermodynamic and kinetic model for paste–aggregate interactions and the alkali–silica reaction, Cem. Concr. Res. 76 (2015) 107–120.

[42] K. Johannsen, S. Rademacher, Modelling the kinetics of calcium hydroxide dissolution in water, Acta Hydrochim. Hydrobiol. 27 (1999) 72–78.

[43] J.L. Palandri, Y.K. Kharaka, A Compilation of Rate Parameters of Water-mineral Interaction Kinetics for Application to Geochemical Modeling, Technical Report, Geological Survey Menlo Park CA, 2004.

[44] A. Leemann, B. Münch, The addition of caesium to concrete with alkali-silica reaction: implications on product identification and recognition of the reaction sequence, Cem. Concr. Res. 120 (2019) 27–35.

[45] A. Leemann, Z.G. Shi, J. Lindgård, Characterization of amorphous and crystalline ASR products formed in concrete aggregates, Cem. Concr. Res. 137 (2020), 106190.

[46] Z.G. Shi, G.Q. Geng, A. Leemann, B. Lothenbach, Synthesis, characterization, and water uptake property of alkali-silica reaction products, Cem. Concr. Res. 121 (2019) 58–71.

[47] Z. Shi, B. Ma, B. Lothenbach, Effect of Al on the formation and structure of alkali-silica reaction products, Cem. Concr. Res. 140 (2021), 106311.

[48] T. Kim, J. Olek, H. Jeong, Alkali–silica reaction: kinetics of chemistry of pore solution and calcium hydroxide content in cementitious system, Cem. Concr. Res. 71 (2015) 36–45.

[49] D. Kashchiev, Nucleation, Elsevier, 2000.

[50] G. Grimmett, D. Stirzaker, Probability and Random Processes, Oxford University Press, 2020.

[51] A. Mersmann, Crystallization Technology Handbook, CRC Press, 2001.

[52] M.R. Andalibi, A. Kumar, B. Srinivasan, P. Bowen, K. Scrivener, C. Ludwig, A. Testino, On the mesoscale mechanism of synthetic calcium–silicate–hydrate precipitation: a population balance modeling approach, J. Mater. Chem. A 6 (2018) 363–373.

[53] D. Kashchiev, G. Van Rosmalen, Nucleation in solutions revisited, Cryst. Res. Technol. 38 (2003) 555–574.

[54] B. Lothenbach, D.A. Kulik, T. Matschei, M. Balonis, L. Baquerizo, B. Dilnesa, G. D. Miron, R.J. Myers, Cemdata18: a chemical thermodynamic database for hydrated Portland cements and alkali-activated materials, Cem. Concr. Res. 115 (2019) 472–506.

[55] J.D. Rimstidt, H. Barnes, The kinetics of silica-water reactions, Geochim. Cosmochim. Acta 44 (1980) 1683–1699.

[56] D. Bulteel, E. Garcia-Diaz, C. Vernet, H. Zanni, Alkali–silica reaction: a method to quantify the reaction degree, Cem. Concr. Res. 32 (2002) 1199–1206.

[57] S. Garrault-Gauffinet, A. Nonat, Experimental investigation of calcium silicate hydrate (CSH) nucleation, J. Cryst. Growth 200 (1999) 565–574.

[58] N. Krautwurst, L. Nicoleau, M. Dietzsch, I. Lieberwirth, C. Labbez, A. Fernandez-Martinez, A.E. Van Driessche, B. Barton, S. Leukel, W. Tremel, Two-step nucleation process of calcium silicate hydrate, the nanobrick of cement, Chem. Mater. 30 (2018) 2895–2904.

[59] M. Kersten, Aqueous solubility diagrams for cementitious waste stabilization systems. 1. The CSH solid-solution system, Environ. Sci. Technol. 30 (1996) 2286–2293.

[60] U.R. Berner, Modelling the incongruent dissolution of hydrated cement minerals, Radiochim. Acta 4 (2) (1988) 387–394.

[61] R. Blaak, P.M. Sloot, Lattice dependence of reaction-diffusion in lattice boltzmann modeling, Comput. Phys. Commun. 129 (2000) 256–266.

[62] S. Diamond, Effects of microsilica (silica fume) on pore-solution chemistry of cement pastes, J. Am. Ceram. Soc. 66 (1983). C–82.

[63] T. Kim, Alkali-silica Reaction: Chemical Mechanism, Thermodynamic Modeling, and Effects of Lithium Ions, Ph.D. thesis, Purdue University, 2013.

[64] S. Multon, A. Sellier, M. Cyr, Chemo–mechanical modeling for prediction of alkali silica reaction (ASR) expansion, Cem. Concr. Res. 39 (2009) 490–500.

[65] X.X. Gao, S. Multon, M. Cyr, A. Sellier, Alkali–silica reaction (ASR) expansion: pessimum effect versus scale effect, Cem. Concr. Res. 44 (2013) 25–33.

[66] X. Hou, L.J. Struble, R.J. Kirkpatrick, Formation of ASR gel and the roles of CSH and portlandite, Cem. Concr. Res. 34 (2004) 1683–1696.

[67] X. Hou, R.J. Kirkpatrick, L.J. Struble, P.J. Monteiro, Structural investigations of alkali silicate gels, J. Am. Ceram. Soc. 88 (2005) 943–949.

[68] T. Kim, J. Olek, Chemical sequence and kinetics of alkali-silica reaction part I. Experiments, J. Am. Ceram. Soc. 97 (2014) 2195–2203.

[69] T. Kim, M.F. Alnahhal, Q.D. Nguyen, P. Panchmatia, A. Hajimohammadi, A. Castel, Initial sequence for alkali-silica reaction: transport barrier and spatial distribution of reaction products, Cem. Concr. Compos. 104 (2019), 103378.

[70] Q. Li, R.J. Kirkpatrick, L.J. Struble, Alkali silica reaction in mortar at room temperature, Spec. Publ. 312 (2016) 1–20.

[71] S. Guo, Q. Dai, R. Si, Effect of calcium and lithium on alkali-silica reaction kinetics and phase development, Cem. Concr. Res. 115 (2019) 220–229.

[72] A. Leemann, C. Merz, An attempt to validate the ultra-accelerated microbar and the concrete performance test with the degree of AAR-induced damage observed in concrete structures, Cem. Concr. Res. 49 (2013) 29–37.

[73] M. Thomas, The role of calcium hydroxide in alkali recycling in concrete, Mater. Sci. Eng. C. Special (2001) 225–236.

[74] T. Ichikawa, M. Miura, Modified model of alkali-silica reaction, Cem. Concr. Res. 37 (2007) 1291–1297.

[75] M. Shakoorioskooie, M. Griffa, A. Leemann, R. Zboray, P. Lura, Alkali-silica Reaction Products and Cracks: X-ray Micro-tomography-based Analysis of Their Spatial-temporal Evolution at a Mesoscale, arXiv preprint arXiv:2105.15092, 2021.

[76] S. Multon, T. de Larrard, F. Duprat, D. Tieudjo, et al., Sensitivity of an alkali-silica reaction kinetics model to diffusion and reactive mechanisms parameters, Constr. Build. Mater. 299 (2021), 123913.

[77] J. Ponce, O. Batic, Different manifestations of the alkali-silica reaction in concrete according to the reaction kinetics of the reactive aggregate, Cem. Concr. Res. 36 (2006) 1148–1156.

[78] L. Sanchez, B. Fournier, M. Jolin, J. Duchesne, Reliable quantification of AAR damage through assessment of the damage rating index (DRI), Cem. Concr. Res. 67 (2015) 74–92.

[79] L.D. Glasser, Osmotic pressure and the swelling of gels, Cem. Concr. Res. 9 (1979) 515–517.

[80] E. Garcia-Diaz, J. Riche, D. Bulteel, C. Vernet, Mechanism of damage for the alkali–silica reaction, Cem. Concr. Res. 36 (2006) 395–400.

[81] M.B. Haha, E. Gallucci, A. Guidoum, K.L. Scrivener, Relation of expansion due to alkali silica reaction to the degree of reaction measured by SEM image analysis, Cem. Concr. Res. 37 (2007) 1206–1214.

[82] G.W. Groves, X. Zhang, A dilatation model for the expansion of silica glass/OPC mortars, Cem. Concr. Res. 20 (1990) 453–460.

[83] Y. Furusawa, H. Ohga, T. Uomoto, Analytical study concerning prediction of concrete expansion due to alkali-silica reaction, Spec. Publ. 145 (1994) 757–780.

[84] C.F. Dunant, K.L. Scrivener, Micro-mechanical modelling of alkali-silica-reaction-induced degradation using the AMIE framework, Cem. Concr. Res. 40 (2010) 517–525.

[85] T. Iskhakov, J.J. Timothy, G. Meschke, Expansion and deterioration of concrete due to ASR: micromechanical modeling and analysis, Cem. Concr. Res. 115 (2019) 507–518.

[86] T. Miura, S. Multon, Y. Kawabata, Influence of the distribution of expansive sites in aggregates on microscopic damage caused by alkali-silica reaction: insights into the mechanical origin of expansion, Cem. Concr. Res. 142 (2021), 106355.

[87] S. Guo, Q.L. Dai, L. Chang, Y. Hu, X. Xie, R. Si, J. Wang, Kinetic analysis and thermodynamic simulation of alkali-silica reaction in cementitious materials, J. Am. Ceram. Soc. 102 (2019) 1463–1478.

[88] A. Leemann, G. Le Saout, F. Winnefeld, D. Rentsch, B. Lothenbach, Alkali–silica reaction: the influence of calcium on silica dissolution and the formation of reaction products, J. Am. Ceram. Soc. 94 (2011) 1243–1249.

[89] G. Geng, Z. Shi, A. Leemann, K. Glazyrin, A. Kleppe, D. Daisenberger, S. Churakov, B. Lothenbach, E. Wieland, R. Dähn, Mechanical behavior and phase change of alkali-silica reaction products under hydrostatic compression, Acta. Crystallogr. B. Struct. Sci. Cryst. Eng. Mater. 76 (2020).

[90] E. Schlangen, Experimental and Numerical Analysis of Fracture Processes in Concrete, Ph.D. thesis, Delft University of Technology, 1995.